Predicting SLS Launch Environment using a Novel Multiphase Formulation

Jordan B. Angel*, Scott Neuhoff†, Man Long Wong‡, Michael F. Barad§, Cetin C. Kiris¶
NASA Ames Research Center, Moffett Field, CA 94035

Powerful acoustic waves generated during ignition of launch vehicles may be dangerous to the vehicle, its payload, or the surrounding structures. The water-based Ignition Overpressure and Sound Suppression (IOP/SS) system at Kennedy Space Center's (KSC) Launch Complex 39B (LC-39B) will be used to protect the Space Launch System (SLS) from the acoustic vibrations generated during launch. The IOP/SS system uses enormous amounts of water to dampen and attenuate these sound waves. To better understand the launch environment risks and to study the effectiveness of the IOP/SS system it is desirable to have time-accurate unsteady simulations of the vehicle ignition with water-based sound suppression. This paper presents results obtained with a novel, high-order accurate, and robust numerical method designed for simulating compressible multiphase flows. A positivity-preserving finite difference scheme is utilized which is formally high-order accurate and also provably robust. Robustness is critical due to the extreme nature of the flow which exhibits highly nonlinear shock and rarefaction waves interacting with liquid-gas interfaces with density ratios of the order of 1000:1. Furthermore, the high-order accuracy (and the high resolution property) is desirable for predicting wave phenomena like IOP waves since the signal can be resolved accurately and propagated long distances with fewer grid points. This finite-difference method was developed using NASA's Launch, Ascent, and Vehicle Aerodynamics (LAVA) Cartesian immersed boundary framework. We present a validation case by applying our solver to the SLS Scale Model Acoustic Test (SMAT). The SLS SMAT is a well-instrumented 5% scale model test meant to represent the SLS at NASA KSC's LC-39B pad. Scale IOP tests were performed with and without the sound suppression water and included many sensors which recorded the pressure waves produced during ignition. For this validation case we conduct two simulations, likewise with and without sound suppression water, and compare the SLS SMAT pressure sensor signals with our numerical signals at identical locations. Following this validation case we present a study of the SLS launch environment to examine engineering safety concerns about the mobile launch pad. Engineers at KSC redesigned the main flame deflector at LC-39B anticipating the increased loads from the SLS and to repair damage from prior Shuttle missions. This deflector redesign made use of surface pressure and temperature data from LAVA full-scale SLS simulations without the sound suppression system. The engineers were questioning the possibility of increased pressure loads on the underside of the mobile launcher due to the water in the flame trench. Based on the results established in our simulations of the SLS SMAT, we performed updated calculations for SLS at LC-39B with and without water systems active to assess the readiness of the launch pad for Artemis I launch. Our results show that the IOP/SS system is effective at reducing the overpressure signal and overall sound pressure levels felt by the vehicle and additionally that the pressure loads experienced by the mobile launcher (ML) during engine startup is not increased by the presence of water.

I. Introduction

Acoustic waves for launch vehicles are primarily composed of low amplitude high frequency waves associated with supersonic shear layers or shock associated broadband noise and high amplitude low frequency waves coming from the

*Computational Aerosciences Branch, jordan.b.angel@nasa.gov
†Computational Aerosciences Branch, scott.neuhoff@nasa.gov
‡Science and Technology Corporation, AIAA Member, manlong.wong@nasa.gov
§Computational Aerosciences Branch, michael.f.barad@nasa.gov
¶Computational Aerosciences Branch, AIAA Senior Member, cetin.c.kiris@nasa.gov

ignition overpressure (IOP) or duct overpressure (DOP) waves. The source of the low frequency high amplitude waves is the piston-like compression of the ambient air from the supersonic plumes during the initial phase of engine firing. The mechanical load associated with these overpressure waves is potentially dangerous to the launch vehicles or its payload. Starting with the Shuttle mission STS-2, water-based sound suppression has been used at NASA Kennedy Space Center (KSC) to dampen these waves as a means of mitigating risk. Figure 1 shows a comparison of pressure signals measured in the solid rocket booster (SRB) exhaust hole for STS-1 which did not use a sound suppression system and STS-2 which used a water-based sound suppression. Clearly the signal is significantly damped for STS-2 compared to STS-1, demonstrating the effectiveness of water-based sound suppression system. In anticipation for the larger acoustic loads from the Space Launch System (SLS), the sound suppression system has been upgraded, Figure 2 shows two photographs of of a test of this water system at Launch Complex 39B (LC-39B). Water-based sound suppression is now common at most launch facilities around the world, however the underlying mechanisms for how they work to suppress sound and the dependence of their effectiveness on parameters like water flow rate are still not well understood. Historically, estimating acoustic loads for launch vehicles has relied on semi-empirical methods augmented with experimental data or scale tests [1, 2]. Though these methods have been improved over the years, they do not give detailed information about the mechanisms that generate the acoustic waves that may be specific to the vehicle or pad and cannot reliably predict the effectiveness of the sound suppression system without additional information from tests. Even still, for decades these methods have been a reliable workhorse for predicting the launch acoustics environment and establishing design criteria to minimize risk to vehicles and payloads. Alternatively, numerical simulations can be used to get much more detailed information about the launch environment. Using a computational framework, it is possible to conduct full-scale simulations of a launch vehicle with complete geometric complexity of the vehicle, pad, and surrounding structures. Furthermore, the data generated by such simulations can be investigated to provide insight into the sound generation mechanisms and peculiarities that may exist for a given vehicle or launch facility. Due to the extreme nature of the flow, robust numerical methods are needed for simulations to remain stable. In practice, low order methods tend to be robust and capable of handling the strong nonlinear waves present in the vehicle plumes but are too dissipative to accurately capture the relatively weak acoustic waves that propagate to the vehicle [3]. Some authors have followed a decoupled approach where the vehicle plume is simulated on one domain with a robust shock-capturing method and the acoustic signal can be solved on another domain with a low-dissipation high-order method [4–6]. However, this introduces an additional complication of coupling the domains and typically the fluid solver is still low order accurate. High-order accurate shock-capturing methods for resolving the plumes and acoustic signals have been used to great effect by others for studying deflector noise and launch acoustics but neglecting the presence of water [7–11]. To our knowledge, there is currently no methodology available for conducting full scale time-accurate predictions of the acoustic loads of a launch vehicle that:

- utilizes high-order (higher than second order) accurate schemes in space and time,
- is robust with provable stability for multiphase simulations that include liquid such as water,
- and is well-validated against known flight or scale test data.

The purpose of this paper is to demonstrate such a capability within NASA's Launch, Ascent, and Vehicle Aerodynamics (LAVA) framework [8]. LAVA is a computational fluid dynamics (CFD) code developed by researchers at NASA Ames Research Center to support NASA projects. To accommodate varied needs of NASA missions, LAVA was designed to support three different grid paradigms: Cartesian adaptive mesh refinement (AMR), unstructured arbitrary polyhedral, and structured overset curvilinear meshes. The LAVA Cartesian grid module has been used successfully in the past for simulations of the KSC launch environment without the water-based sound suppression system. These simulations solve the multispecies Navier–Stokes or Euler equations that model the air and the vehicle's exhaust as a mixture of ideal gases [8, 12]. In this paper we demonstrate the new capability within this framework to solve equations of motion for a multi-fluid flow model that can model liquid water and remove the restriction of an ideal gas mixture. The flow model assumes that there are multiple immiscible fluids, described by stiffened gas or ideal gas equations of state. Each fluid obeys its own conservation of mass equation with additional conservation equations for mixture momentum and energy. The numerical treatment of this model is robust and has high resolution due to high order of accuracy. The high resolution property is beneficial in the current problem because fewer grid points are required to resolve the acoustic waves or diffuse material interfaces. To achieve this we have already developed a new numerical scheme [13] with extension to a liquid with many gases that is high-order accurate for flows in smooth regions and provably positivity-preserving which guarantees the robustness of the simulations. This numerical scheme has been incorporated into the LAVA Cartesian module. Section II provides a brief description of the multiphase flow model and its numerical discretization.

The SLS Scale Model Acoustic Test (SMAT) will serve as a validation case for the multiphase solver. This is a

well-instrumented 5% scale test meant to represent the SLS at KSC's LC-39B. The SLS SMAT had both dry and wet rocket firings with varying vehicle positions and flow rates for the water system. In this paper we consider two of these test firings with the test vehicle in a hold-down position to model IOP conditions for the SLS. The setup for these test are identical except that one was fired with a scaled sound suppression system and the other was fired without water. Section III presents the results of these two validation cases by comparing our numerical pressure signals with measurements taken at the scale test.

Based on the results of our simulations of the SLS SMAT, we perform update calculations for SLS at LC-39B with and without water systems active to assess the readiness of the launch pad for Artemis I launch. These simulations were conducted to address a concern that flame trench water could lead to an increase in pressure loads on the mobile launcher (ML). Section IV presents the results of the SLS simulations and shows our pressure signals and overall sound pressure levels at some representative locations on the vehicle body and ML. In section V we give a brief discussion of the current status of the computational framework and outline further simulations that will come in the future.

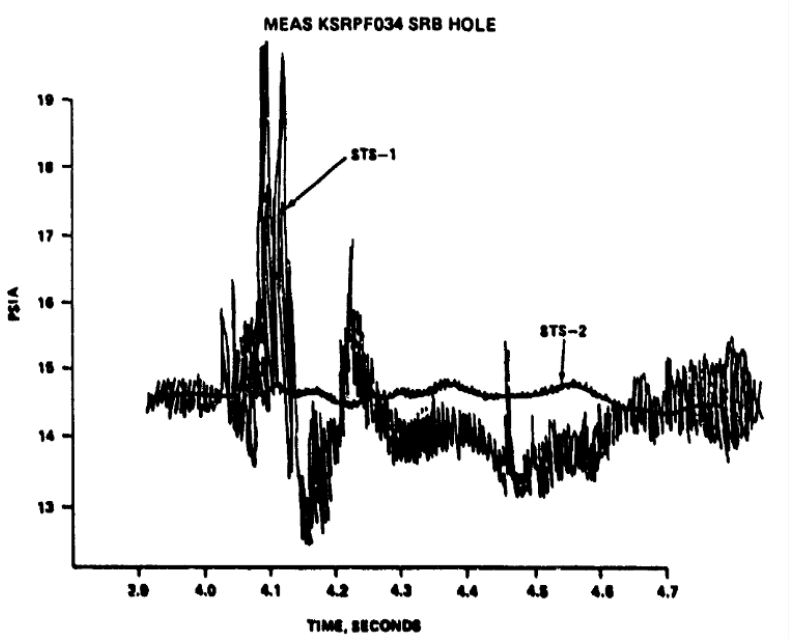

Figure 38. Shuttle overpressure data on LC39 launch facility.

Fig. 1 Comparison of pressure signals measured in SRB exhaust hole for STS-1 and STS-2 [14]. Water-based sound suppression was introduced in STS-2.

II. Multiphase Model and Discretization

The multiphase formulation is based on the hyperbolic five-equation flow model of Allaire et al. [16] with additional thermal and thermo-chemical relaxation steps [17]. For N species, the system of equation without any relaxation terms is given by

$$\partial_t (\alpha_k \rho_k) + \nabla \cdot (\alpha_k \rho_k \mathbf{u}) = 0, \text{ for } k = 1, \ldots, N \tag{1}$$

$$\partial_t (\rho \mathbf{u}) + \nabla \cdot (\rho \mathbf{u} \otimes \mathbf{u}) + \nabla p = 0, \tag{2}$$

$$\partial_t E + \nabla \cdot [(E + p)\,\mathbf{u}] = 0, \tag{3}$$

$$\partial_t \alpha_k + \mathbf{u} \cdot \nabla \alpha_k = 0, \text{ for } k = 1, \ldots, N-1. \tag{4}$$

There are $2N + D$ equations for D spatial dimensions and $\mathbf{u}$ and p are the velocity vector and the pressure of the mixture respectively. Additionally, α_k and ρ_k denote respectively the volume fraction and species density of species k. The partial densities of species k are $\alpha_k \rho_k = \rho Y_k$ where ρ is the mixture density and Y_k is mass fraction of species k. The

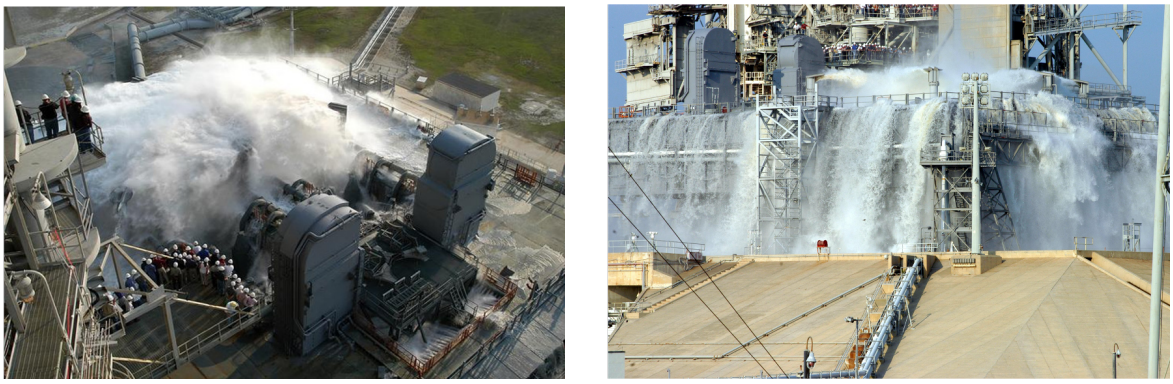

Fig. 2 Photographs showing a test of the water deluge system at KSC LC-39B [15].

mixture total energy per unit volume is $E = \rho(e + |\mathbf{u}|^2/2)$ where e is the mixture specific internal energy. All species are assumed to be at the same mixture pressure, p, which is assumed to be the equilibrium thermodynamic pressure. Each constituent species obeys a modified stiffened gas equation of state,

$$\frac{p + \gamma_k p_k^\infty}{\gamma_k - 1} = \rho_k (e_k - q_k). \tag{5}$$

The temperature of species k is given by

$$T_k = \frac{p + p_k^\infty}{(\gamma_k - 1)\,\rho_k c_{v,k}}, \quad \gamma_k = \frac{c_{p,k}}{c_{v,k}}. \tag{6}$$

For non-liquid species, the parameter p_k^∞ is zero and the equation of state is that of an ideal gas but for liquids p_k^∞ is a large positive number and effectively makes the species behave more like an incompressible fluid. An explicit equation for pressure can be derived by multiplying Equation (5) by α_k and summing over k. The system also has the following constraints,

$$\sum_{k=1}^{N} \alpha_k = 1, \qquad \sum_{k=1}^{N} \alpha_k \rho_k = \rho, \qquad \sum_{k=1}^{N} \alpha_k \rho_k e_k = \rho e. \tag{7}$$

This closes the system of equations. A discussion of the mathematical properties of this system can be found in [16].

A. Robust High-Order Spatial Discretization

Our high-order discretization of the equations of motion follows a method-of-lines approach where the flux and velocity divergences are discretized with a hybrid midpoint-and-node differencing scheme. The high-order fluxes and velocities at cell midpoints are calculated with a modified Harten-Lax-van Leer contact (HLLC) Riemann solver using left- and right-biased incremental-stencil Weighted Essentially Non-Oscillatory (WENO) interpolated variables. The overall scheme belongs to the Weighted Compact Nonlinear Scheme (WCNS) family [18–21]. The overall spatial order of accuracy is fifth order for smooth solutions. The discretization in time follows the Strong Stability Preserving Runge-Kutta third order (SSP-RK3) formulation [22]. This makes the overall method fifth order accurate in space and third order accurate in time.

As we previously stated, for launch environment predictions a robust numerical method is essential due to the extreme nature of the flow. To achieve this we have developed an overall positivity-preserving scheme that, under a suitable Courant–Friedrichs–Lewy (CFL) limit of 0.5, can maintain the positivity of the partial densities ($\alpha_k \rho_k > 0$), the boundedness of the volume fractions ($0 < \alpha_k < 1$), and the positivity of the mixture squared speed of sound ($c^2 > 0$). The details of the numerical method for gas-liquid flows can be found in [13].

B. Phase Transition Model

A phase transition model is used to account for the vaporization of liquid water by the hot rocket exhaust. The model determines whether the water in the mixture with the inert ideal gases is super-heated water vapor, sub-cooled

liquid water, or at saturation state. When the water is determined to be at saturation state, a state at thermo-chemical equilibrium with single mixture pressure and mixture temperature is computed such that the liquid phase and vapor phase have equivalent Gibbs free energies. The Gibbs free energy of species k is given by

$$g_k\left(p_k, T_k\right) = \left(\gamma_k c_{v,k} - q'_k\right) T_k - c_{v,k} T_k \ln\left[\frac{T_k^{\gamma_k}}{\left(p_k + p_k^{\infty}\right)^{\gamma_k - 1}}\right] + q_k. \tag{8}$$

The phase transition model effectively accounts for liquid to vapor or vapor to liquid transition. The properties of the liquid water and water vapor are given in Table 1. Note that with these properties, the liquid density is close to 1000 kg m^{-3} under ambient conditions. Instead of an exact thermo-chemical relaxation step that requires nonlinear solve, an algebraic step modified from the approximate method in [23] with improved robustness is used. The overall time advancement follows a fractional step approach with the hyperbolic system being advanced first, then the phase transition step, for each Runge–Kutta substep.

Fluid	γ_k	$c_{p,k}$ (J kg^{-1} K^{-1})	p_k^{∞} (Pa)	q_k (J kg^{-1})	q'_k (J kg^{-1} K^{-1})	W_k (g mol^{-1})
Liquid water	2.35	4267.6	1.0×10^9	-1.167×10^6	0	18.0
Water vapor	1.43	1487.2	0	2.030×10^6	-2.34×10^4	18.0

Table 1 Equation of state parameters for liquid water and water vapor. These values are found in [24].

C. Approach for Launch Environment Simulations

Our multiphase solver is implemented within LAVA's Cartesian adaptive mesh refinement (AMR) module. This module solves the discretized equations on a rectangular Cartesian mesh with multiple properly nested refinement regions of isotropic cells. The Cartesian AMR module was chosen for the following reasons:

- The launch environment simulations enclose a very large domain, the nested refinement levels is a convenient way to save grid points and increase resolution where it is needed.
- The logical data layout for uniform meshes make the numerical implementation more efficient, especially for high-order nonlinear schemes that make frequent use of neighboring cell data.
- Launch vehicles and launch environments typically have very complicated geometry. An immersed boundary ghost-cell approach allows us to start from a water-tight CAD to generate a surface triangulation without manual grid generation.
- We are interested in IOP wave propagation which is a largely inviscid phenomena, so we do not resolve viscous boundary layers near walls which could very expensive for isotropic cells.
- Isotropic cells in the Cartesian framework are more optimal for wave propagation than cells with non-unit aspect ratio.

III. SLS Scale Model Acoustic Test (SMAT) Validation

To investigate the applicability of the multiphase solver for making IOP predictions, we consider the SLS Scale Model Acoustic Test (SMAT). The SLS SMAT is a 5% scale test conducted at NASA Marshall Space Flight Center which was designed to represent the SLS launch from Launch Complex 39B at NASA Kennedy Space Center. The test used a scaled vehicle, mobile launch pad, flame trench, and support structures. Figure 3 shows a photograph of the experimental test setup at Marshall Space Flight Center. The test vehicle utilized four liquid engines meant to model the RS-25 core engines on the SLS and two solid rocket motors to model the SLS solid booster engines. The pad and flame deflector also incorporates a scaled water-based sound suppression system with appropriately scaled water flow rates. By varying setup conditions such as vehicle elevation above the pad, pad water flow rate, and vehicle drift positions, many test firings were conducted and pressure recordings taken. Scale tests like the SLS SMAT can provide information to engineers about the potential IOP wave, the effectiveness of the sound suppression system, and the readiness of the launch pad. Dozens of pressure sensors were placed on the test vehicle, pad, and support structures and these recorded pressure signals will be used as a validation metric for our simulations. Due to the highly unsteady nature of the pressure

Fig. 3 Photograph of the SLS Scale Model Acoustic Test (SMAT) during an elevated vehicle case meant to model vehicle lift-off [25].

signals, it is more useful to compare moving averages. We calculate a moving average for pressure as

$$\langle p \rangle(t) = \frac{1}{\Delta t} \int_{t-\frac{\Delta t}{2}}^{t+\frac{\Delta t}{2}} p(\tau)\, \mathrm{d}\tau, \tag{9}$$

where Δt is given by $\Delta t = L/c_{air}$ with c_{air} being the speed of sound of air and L a characteristic length scale. We also compute the root mean square (RMS) in a pointwise fashion using the moving average given by Equation (9),

$$p_{\mathrm{RMS}} = \sqrt{\langle p^2 \rangle - \langle p \rangle^2}. \tag{10}$$

Our results will compare the moving average and RMS of the recorded signal and the data from numerical probes placed at identical locations, however due to restrictions on the experimental data our plots cannot include numerical values and must be interpreted qualitatively. Additionally, we are only able to compare to a small subset of the pressure sensors used in the scale test based on what was made available to us and some probes were excluded due to sensor failures.

We consider two specific test firings of the SLS SMAT where the vehicle is in the hold down position as the SLS would be during ignition. These firings were conducted to measure IOP waves specifically. In the first case, the sound suppression water system is completely off producing a *dry fire case*. This dry fire case is useful for validating certain aspects of the computational setup that are independent of the multiphase solver itself. We will use this dry fire case to check that we are getting acceptable results from our nozzle boundary conditions and computational mesh. The second case we consider is a *wet fire case*. In this case, the water system is actively injecting large amounts of water into the pad

exhaust hole and from the top of the flame deflector. The water system will be included in our simulations by using mass flow boundary conditions in the location of water inlets.

Figure 4 shows the surface geometry of the SLS SMAT test vehicle, pad, and support structures. This geometry is included in our Cartesian simulations using an immersed boundary ghost cell procedure. Our simulation with the sound suppression water includes the flame deflector water inlet and the exhaust duct water inlets but does not use the "rainbirds" seen in this figure, which is consistent with the test fire we are modeling. Figure 5 shows a planar slice of the computational mesh for our simulations with the computational geometry shown in white. The inset figure depicts the mesh inside the flame trench and near the vehicle nozzles. These simulations utilize 8 levels of refinement with the finest mesh resolution equal to approximately 50 cells per solid booster nozzle diameter. As a representative simulation picture, Figure 6 shows a view of pressure on a planar slice depicting wave structures typical during solid booster ignition. Numerical sensor locations are shown as yellow dots and are placed according to the distribution of physical sensors in the test.

A. Simulation Setup - Boundary Conditions

For both cases we will need accurate boundary conditions for the test vehicle engines. Because we are working in a Cartesian framework, simulating the internal engine flow could be very costly since the geometric details of the nozzle interior are quite small compared to the overall computational domain and therefore would require very small cells to resolve accurately. Instead of including the engine internals in our Cartesian simulations, we first use LAVA's unstructured grid solver to conduct high-resolution simulations of the engines and use the results from these simulations to provide boundary conditions at the nozzle exit planes in our Cartesian simulations.

The solid booster motors drive the IOP wave generation and must be modelled with an accurate time history since the strength of the IOP wave will depend on the pressure rise rate of the engine. We include these engines in our Cartesian simulations by imposing a time-dependent boundary condition on the ghost-cells near the nozzle exits. We generate these boundary conditions by first making use of LAVA's unstructured grid solver to conduct high-resolution simulations of the motor interiors. The unstructured code can easily generate a high quality mesh for the nozzle geometry and the simulations are inexpensive since the domain is relatively small and axisymmetric. Strain gauges took time-dependent measurements of each solid booster casing which we use to estimate the motor's chamber pressure. This time-accurate chamber pressure data is imposed as a boundary condition along with estimated chamber temperature as the second thermodynamic property and stagnation conditions for velocity. By imposing chamber conditions in the mixing chamber, we simulate the internal flow of the solid engine nozzle and the solid booster nozzle and extract data along the nozzle exit.

The liquid engines spend much more time at full thrust compared with the solid engines, about ten times the duration of the IOP window we are interested in capturing. Since the liquid engines are not directly contributing to the IOP wave generation, it is not necessary to have time-accurate information for their startup. With this in mind, our Cartesian simulations use full thrust conditions for the liquid engines that are constant in time but still radially varying. We generate the liquid engine nozzle exit conditions by imposing the steady chamber pressure and temperature at full thrust opposed to the time-dependent chamber conditions used for the solid motors. These simulations are solved to steady-state and exit conditions are extracted the same way as the solid booster engines.

Pressure sensors from the scale test indicate that the pressure environment is statistically stationary about the ambient pressure when the solid engines are fired. Since the liquid engine boundary conditions are started at full thrust, there is a nonphysical wave generated by their spontaneous ignition which must propagate out of the domain. Once this transient startup wave has left the domain and the environment is quasi-steady, the solid booster motors are started and the physical time is marked as $t = 0$.

B. SLS SMAT Without Water Sound Suppression

First, we consider the dry case which was fired without any water systems active. Comparing to a dry case allows us to validate the geometry and the engine boundary conditions independent of the multiphase capability and water modeling challenges. As discussed, the liquid engine boundary conditions are started with their steady-state full thrust values which creates an impulsive wave that is nonphysical and must be allowed to propagate out of the domain before starting the solid engines which are the primary driver of the IOP wave. Once the solid boosters are started, we mark the physical time as $t = 0$ to align our simulation results with the recorded pressure signals. Figure 7 shows pressure sensor comparisons for sensors located on the test vehicle body. There is a clear propagation of the overpressure waves up the vehicle body which is seen in the recorded and numerical data. Overall, we observe good agreement between the

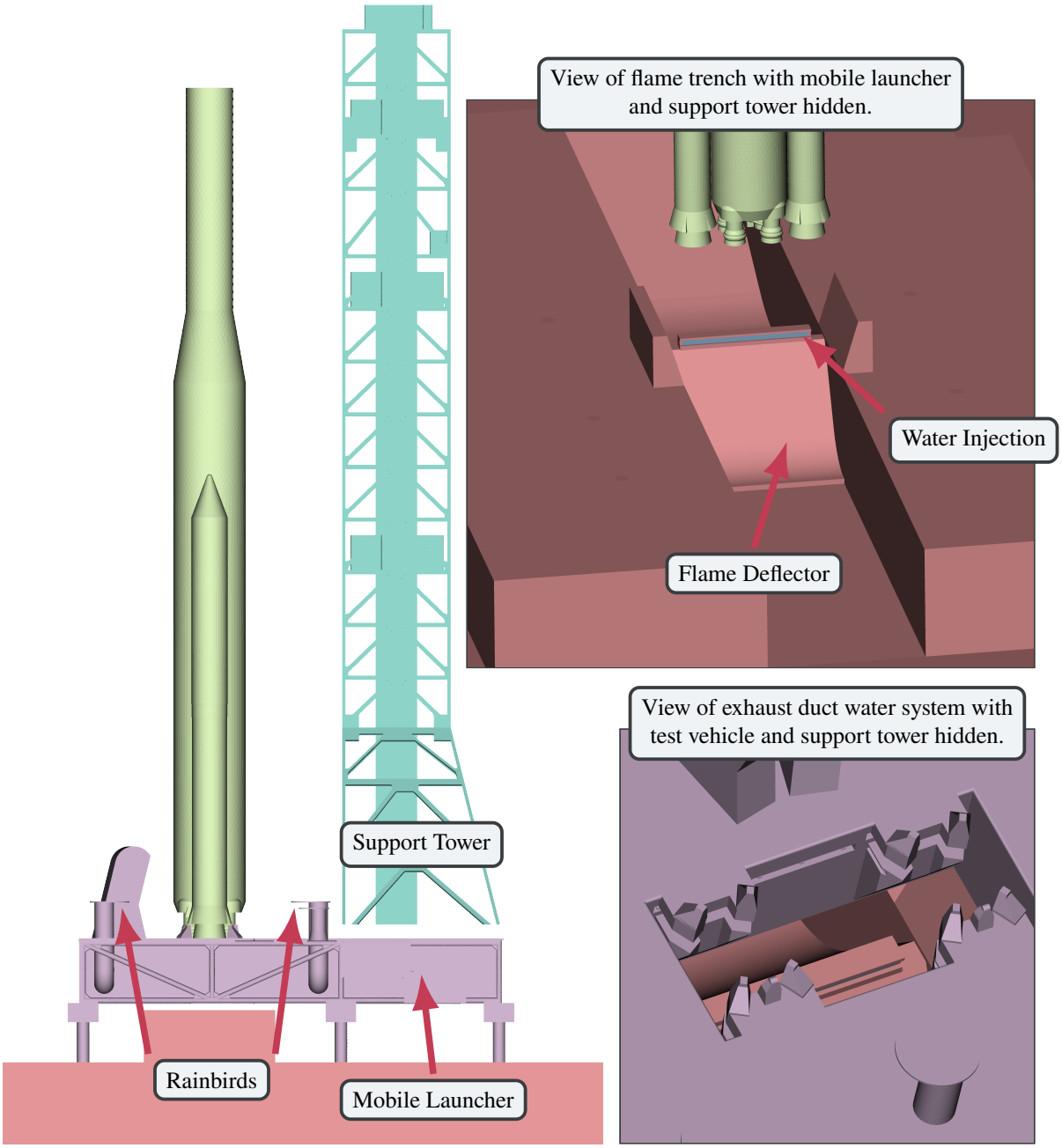

Fig. 4 Simplified computational geometry for the SLS SMAT test vehicle, pad, and support structures. Left: Sideview showing vehicle, pad, and tower. Top Right: View of trench and flame deflector with deflector water inlet. Bottom Right: View of exhaust duct with core and booster water inlets.

numerical and recorded pressure signals for these sensors but we note that there is a small discrepancy at the leading portion of the IOP signal. Figure 8 shows comparisons for two sensors on the underside of the ML that covers the flame trench. In this location we see much larger RMS compared to variations in the moving average pressure which indicates noisy high frequency pressure fluctuations in the trench. The signals match each other closely with the numerical signal showing similar high frequency fluctuations compared to the fluctuations in the mean. Finally, Figure 9 shows results for probes inside the flame trench and on the flame deflector. The top and middle plots correspond to probes in two very challenging locations: one on the flame deflector below a solid booster and one just in front of the step at the base of the deflector. In these regions the flow is strongly nonlinear due to standing shocks on the deflector and strong

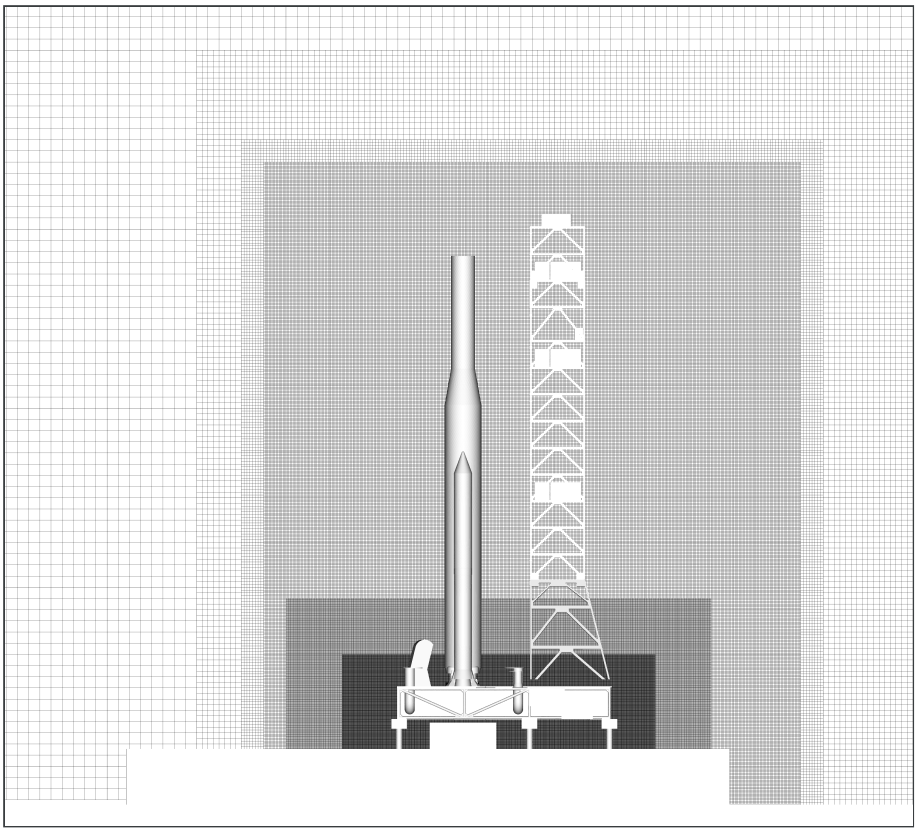

Fig. 5 Visualization of the compuational mesh used for the SLS SMAT simulations. Our finest grid resolution is concentrated at the engine nozzles with gradual coarsening away from the region of interest to save computational resources.

expansion waves at the deflector base step which makes predictions here very sensitive to spatial location. For the probe on the deflector, the test data shows a suspiciously small RMS and which may indicate an issue with this sensor as some other sensors were known to have errors but we are not prepared to rule it out. Our numerical results show a much earlier onset of pressure rise due to the impingement of the booster plume and a large variation of the signal at the peak which may be due to unsteady motions of the standing shocks here. The probe below the deflector step resides in an area of very strong expansion which is evident in the sudden drop in pressure seen in both the numerical and recorded pressure signals. There is an offset in the pressure magnitudes comparing the numerical and recorded signals however the onset of the pressure drop due to the flow expansion seems to be well captured. Both signals also show good agreement in RMS. The bottom plot corresponds to a probe that is away from the flow of the plumes and the shocks and expansion waves associated with the deflector. Qualitatively, there is good agreement between the fluctuations of the moving averages however we note that the numerical signal is slightly lower across the entire duration. Based on the comparisons we have presented, we find that the agreement between sensors is very favorable and gives us confidence in our boundary conditions and computational mesh for the scale test.

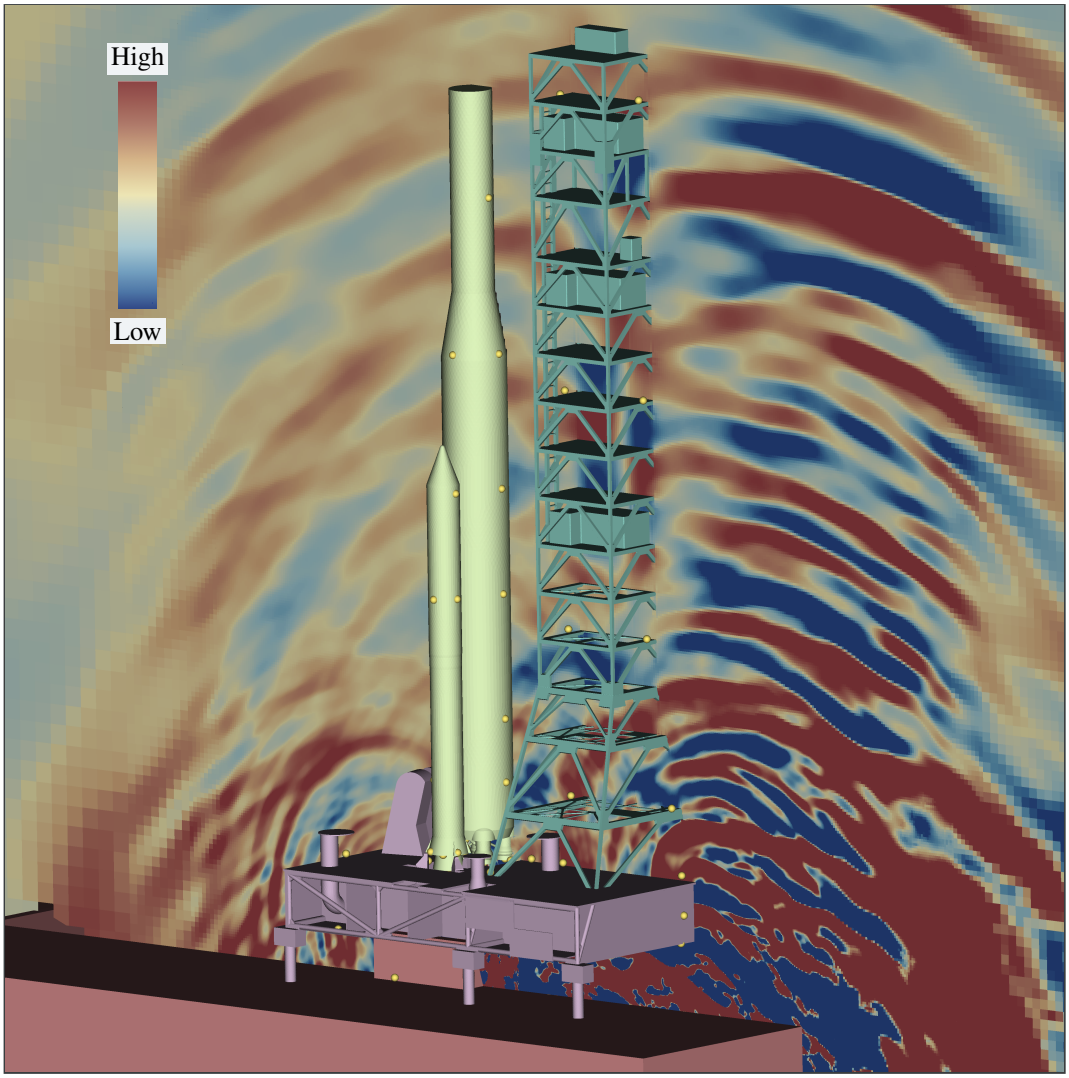

Fig. 6 Visualization of pressure on a slice through the computational domain, red indicates high pressure and blue indicates low pressure. Locations of numerical probes shown by yellow dots.

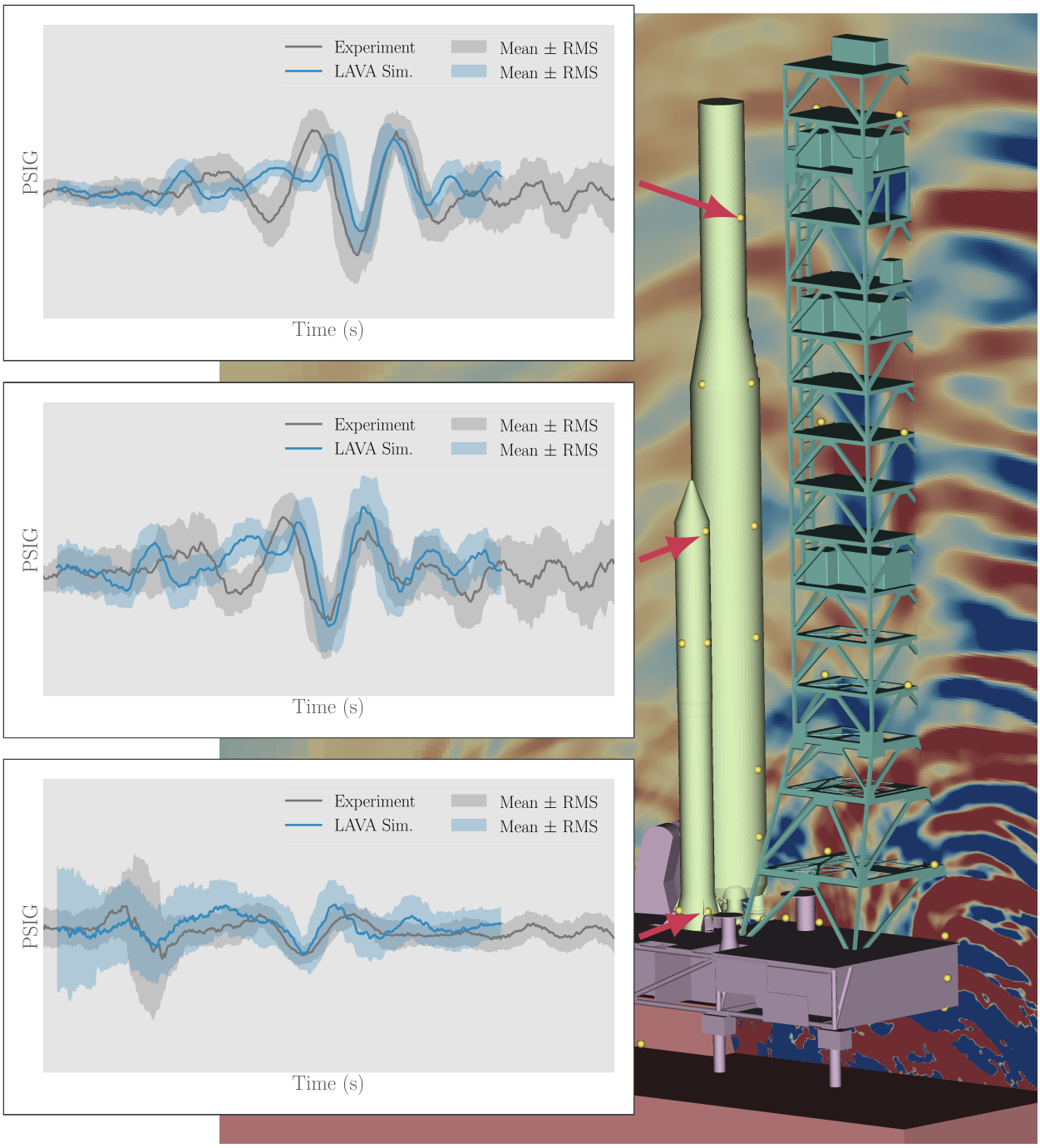

Fig. 7 Comparison of pressure signals for the dry fire case on the vehicle body. Experimental results are shown in dark gray. Numerical results are shown in blue.

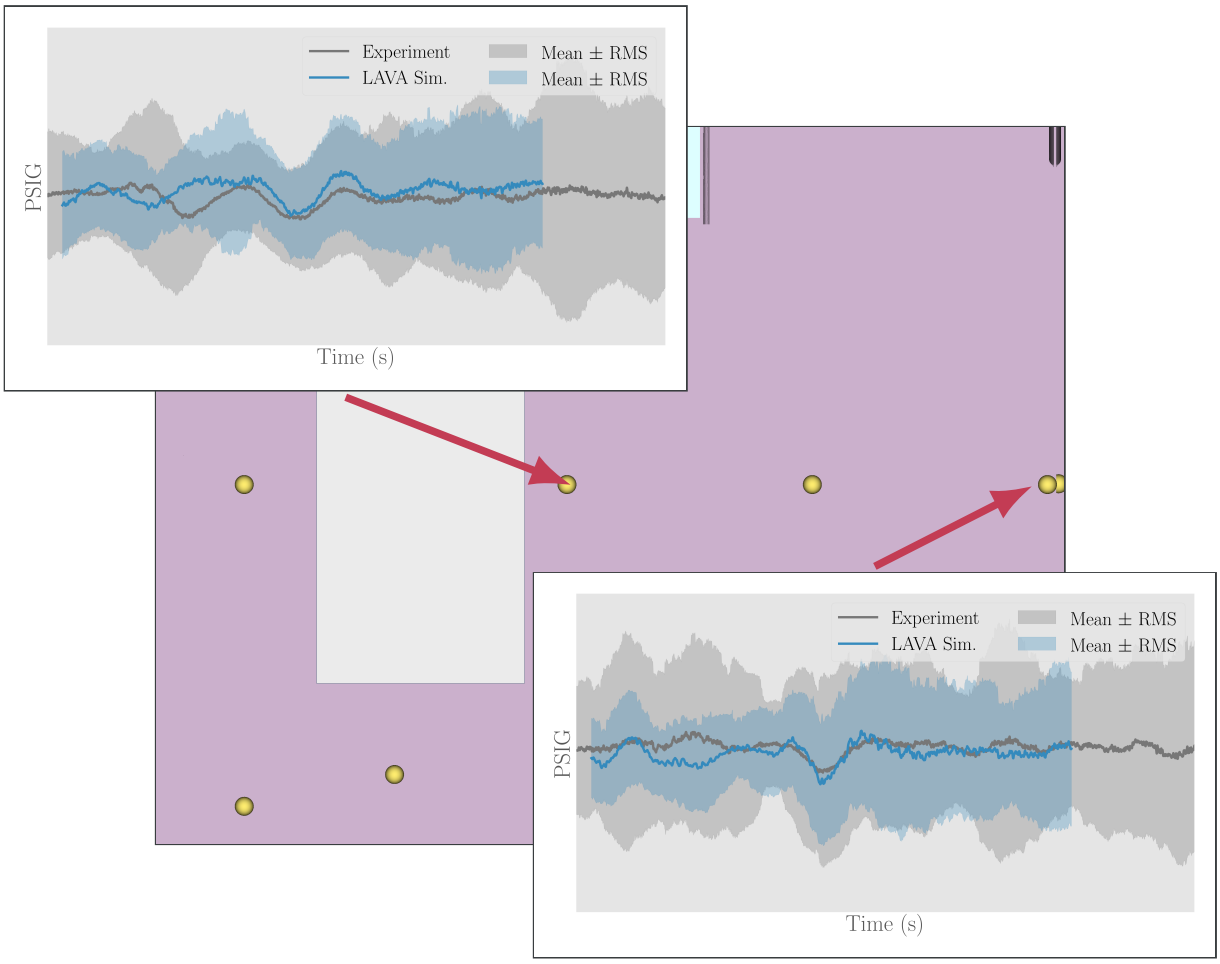

Fig. 8 Comparison of pressure signals for the dry fire case on the underside of the launch pad. Experimental results are shown in dark gray and numerical results are shown in blue.

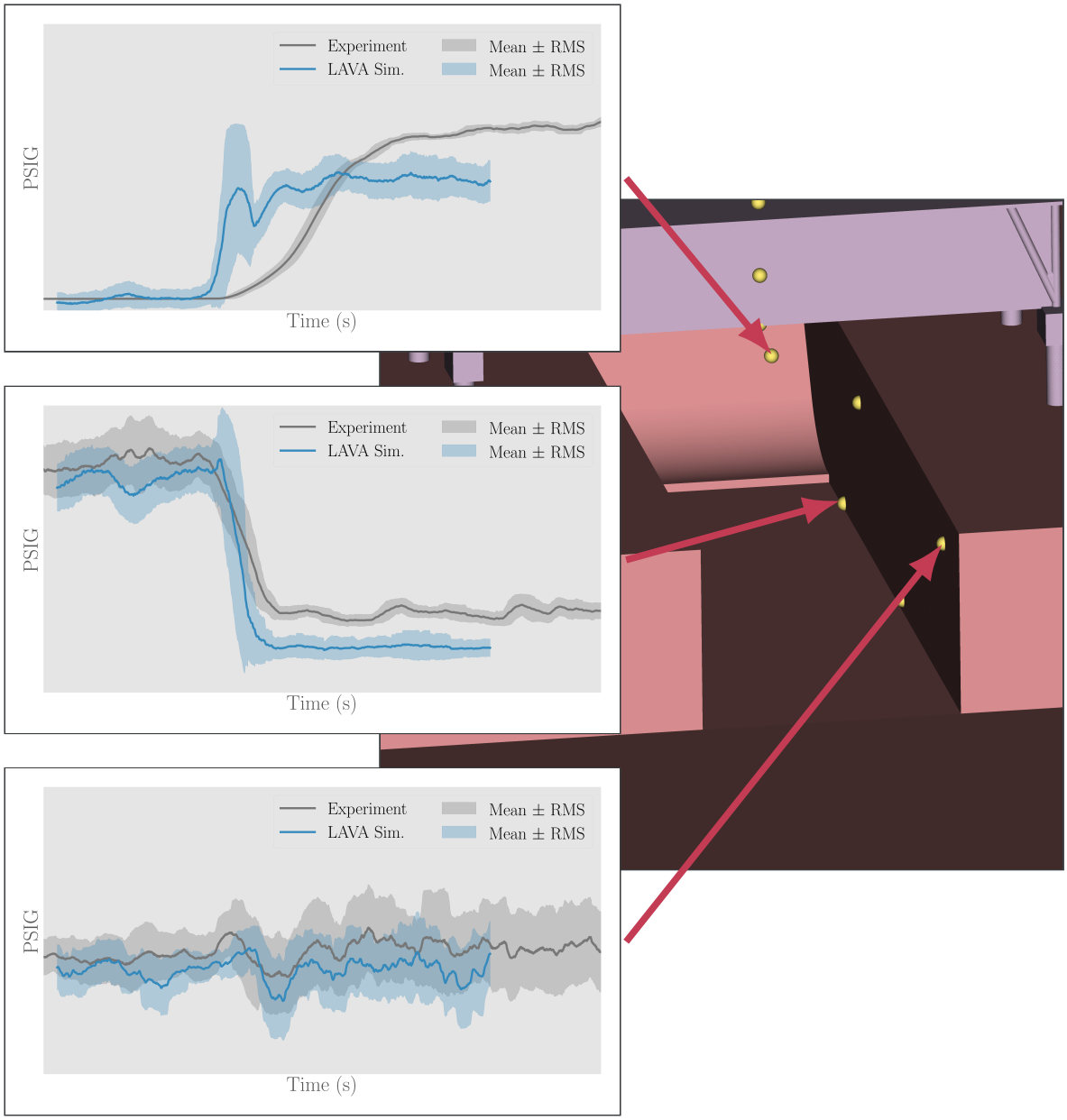

Fig. 9 Comparison of pressure signals for the dry fire case in the flame trench and on the flame deflector. Experimental results are shown in dark gray and numerical results are shown in blue.

C. SLS SMAT With Water Sound Suppression

Next, we consider the wet case which incorporates the sound suppression water in the exhaust duct and on the top of the flame deflector. These are seen in the inset images in Figure 4. The SLS SMAT water system also includes rainbirds located on the top of the pad but for this particular firing they were off so we neglect them here. To include the water flow in our simulations, we impose mass flow boundary conditions at the exhaust duct inlets and on the flame deflector. In terms of modeling, the wet case presents a unique challenge. During the test, the water system is started multiple seconds before the liquid engines. Prior to motor ignition, the flow is mostly incompressible and low speed. This presents a challenge for our numerical framework which is formulated specifically with compressible flow in mind. Our explicit time step is limited by the acoustic CFL number which makes long time integrations computationally expensive. It is not practical to simulate the water system for multiple seconds before starting the liquid engines. Instead, we initiate the water system and the liquid engines simultaneously knowing we will have to wait for the transient waves to leave the domain. This procedure allows some time to the water system to produce coverage of the exhaust duct and trench but it is difficult to measure whether the coverage of water is captured accurately. The spatial distribution of water at the time of booster ignition is probably the largest source of uncertainty in our modeling of this test.

Figure 10 shows three pressure sensor comparisons at the same locations as those shown in the dry case in Figure 7. Starting from the probe closest to the base of the vehicle, we notice that early in time there is a distinct pressure wave which is too early to be attributed to the solid boosters. Based on discussions with test engineers we attribute this peak to the solid engine igniter which we have not modeled here and do not expect to capture this pulse. This comparison also shows some regions where the mean pressure deflects from the experiment and overall the numerical signal show a larger RMS compared to the measured data. Looking at the sensors further up the vehicle body, a good match is seen in mean pressure and RMS early in time just before the arrival of the IOP signature but we see that the numerical results predict a weaker peak IOP strength with a stronger drop in pressure compared to the experiment. The numerical results do show an attenuation of the IOP wave and reduced RMS compared to the dry simulations, but not to the same degree observed in the test. In Figure 11 we show comparisons on the underside of the ML at the same locations as shown in Figure 8 but with an additional probe included which we did not have data for in the dry fire case. The first observation is that the RMS is much larger in the numerical simulation compared to the recorded signals. We interpret this as an indication that we do not have sufficient water coverage in the trench compared to the experiment. As for the mean pressures, starting from the top plot we see that the numerical results experience some overpressure but smaller magnitude compared to the experiment, then the signal follows the decrease in pressure accurately but experiences a second rise in pressure before returning to experimental values. The middle plot is indicating a similar situation where the peak of the over pressure is underestimated then the drop in pressure is captured with some rise following before settling back close to the recorded signal. The last plot in this figure shows our predictions of the mean pressure signal agree well with the test in amplitude, but with a slight shift in arrival time. Next, we return to the flame trench probes in Figure 12 but this time without the probe on the deflector since it failed to record a signal during the test. The top plot corresponds to the probe below the flame deflector step where there is a strong expansion wave as we noted previously. The numerical results in this case make a large over prediction of maximum pressure before dropping down to the recorded signal level. Closer to the trench exit and away from the strong shock and expansion waves we observe better agreement noting a similar RMS but a distinct larger pressure wave seen in the test signal is missing from the simulation results. Lastly, we turn to a probe in the exhaust duct shown in Figure 13 which we did not have available for our dry run. Early in time we see a pulse in the test data which we attribute to the solid booster igniter as discussed earlier which seems likely given the proximity of this sensor to the booster nozzle. After this pulse the signals agree well in both mean and RMS and both seem to show a drop in pressure likely due to entrainment from the booster plume before returning to equilibrium levels. This probe may be less sensitive to the initial distribution of water because of its location in the exhaust duct.

Our comparison with this case is less favorable than the previous dry case but the results do show the typical IOP phenomena and attenuation due to the sound suppression water with reasonable accuracy. Incorporating the sound suppression system introduces considerable complexity in the flow due to the chaotic interaction of the water with the liquid engine plumes prior to booster ignition. Overall, the results with sound suppression water are encouraging but more work is needed to improve our water system modeling for this case.

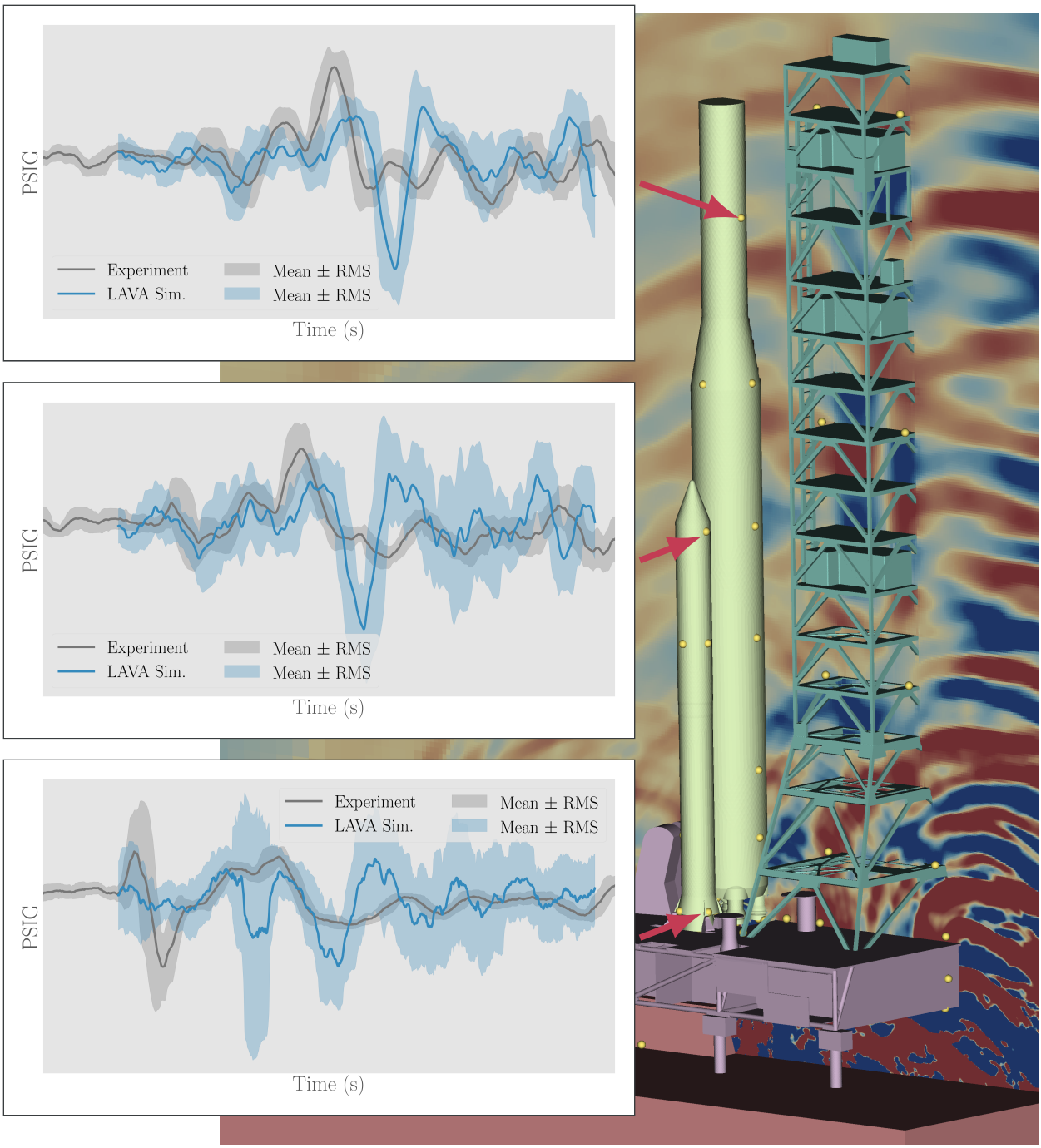

Fig. 10 Comparison of pressure signals for the sound suppression case on the vehicle body. Experimental results are shown in dark gray. Numerical results are shown in blue.

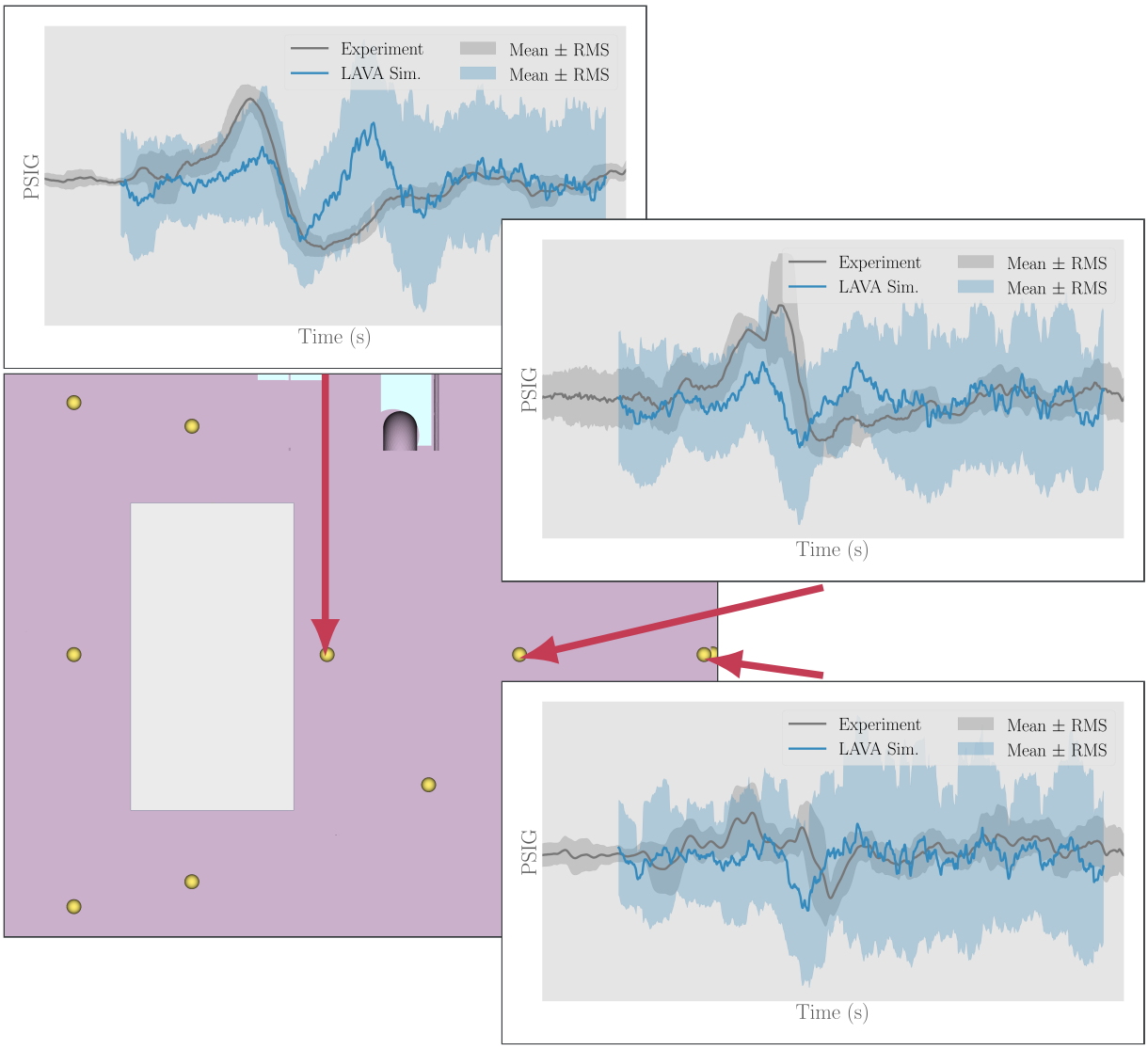

Fig. 11 Comparison of pressure signals for the sound suppression case on the underside of the launch pad. Experimental results are shown in dark gray. Numerical results are shown in blue.

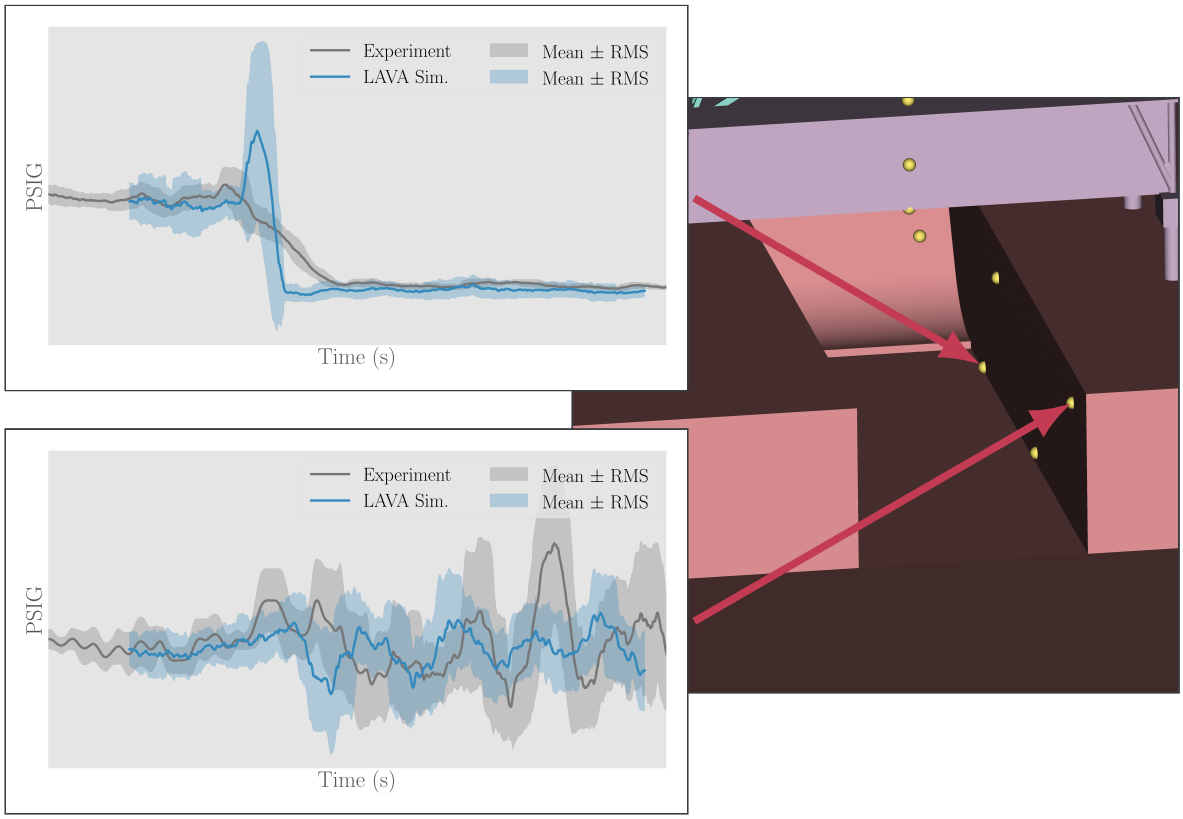

Fig. 12 Comparison of pressure signals for the sound suppression case in the flame trench and on the flame deflector. Experimental results are shown in dark gray. Numerical results are shown in blue.

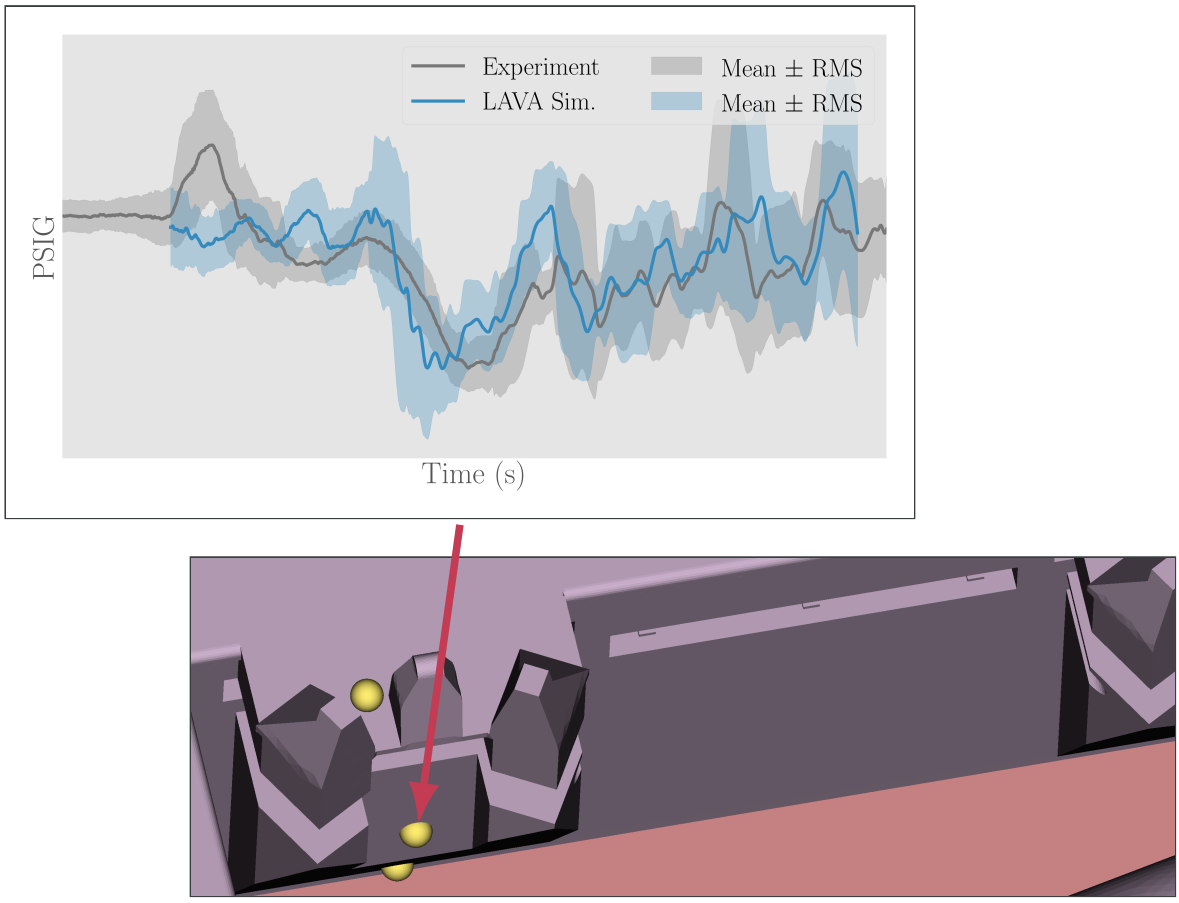

Fig. 13 Comparison of pressure signals for the sound suppression case in the exhaust duct of the launch pad. Experimental results are shown in dark gray. Numerical results are shown in blue.

IV. Space Launch System (SLS) at KSC LC-39B

Prior to Artemis I an issue was brought forward by engineers concerning the interaction between the vehicle plumes and the sound suppression water in the flame trench. There was a concern that the underside of the mobile launch pad could could experience extreme over pressures that could pose a safety risk for the mission. Following the SLS SMAT validation study, there was a request to apply the LAVA multiphase solver to simulate the full-scale SLS Artemis I conditions and provide KSC engineers with surface pressure data so they could make a risk assessment. KSC provided computer-aided design (CAD) models for the launch facility, the mobile launch pad, and the SLS vehicle which can be seen from a bird's eye view in 14.

Similar to the SLS SMAT simulations, we first simulate the SLS without any of the water systems active and then we repeat the simulation with the water systems included. The purpose of including a dry case for the SLS is to observe the effect the sound suppression water an ensure that the water does not make conditions worse on the mobile launch pad. These simulations were performed prior to the Artemis I flight so there was no data to assess accuracy however we plan to make these comparisons when that data is available. The sound suppression systems included in this study are spray nozzles at the top of the flame deflector and the water injection nozzles in the exhaust duct just beneath the vehicle. The upright rainbirds atop the mobile launch pad platform are excluded here as they were in the scale test since their ejected water does not directly interact with the engine plumes in the time of interest. Figure 15 shows a volume rendering of a snapshot from the simulation that includes the sound suppression water. It shows the water (blue) coming from the exhaust duct and flame deflector interacting with the solid booster plume (yellow/purple) and producing water vapor (white).

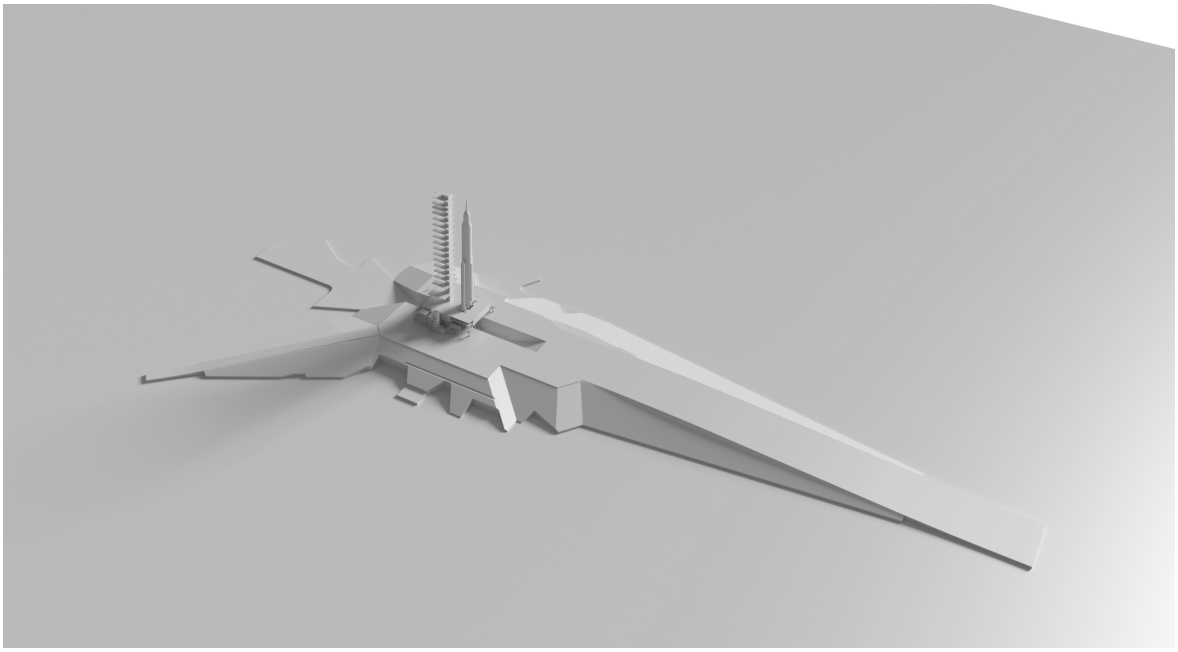

Fig. 14 Bird's eye view of the computational geometry used for the SLS simulations.

Figure 16 shows moving mean and RMS for pressure signals at three points on the vehicle body in similar locations corresponding to the sensors from the SLS SMAT study seen in Figure 7. Starting from the bottom plot we observe the dry simulation shows a larger amplitude IOP wave and much larger RMS which is consistent with the SLS SMAT findings. The middle plot in the figure shows results for a sensor near the top of the solid booster. At this location we observe much less high frequency noise compared to the bottom sensor and a very clear IOP signal for both simulations. The IOP for the case with sound suppression water shows a significantly reduced amplitude and an attenuated wave form. Finally, the top plot shows results for a sensor placed near the payload area. Here the effect of the sound suppression water is even more pronounce with the wet case showing a significantly diminished IOP compared to the dry case. These results provide confidence that the water in our simulations is having the intended effect of reducing the IOP wave

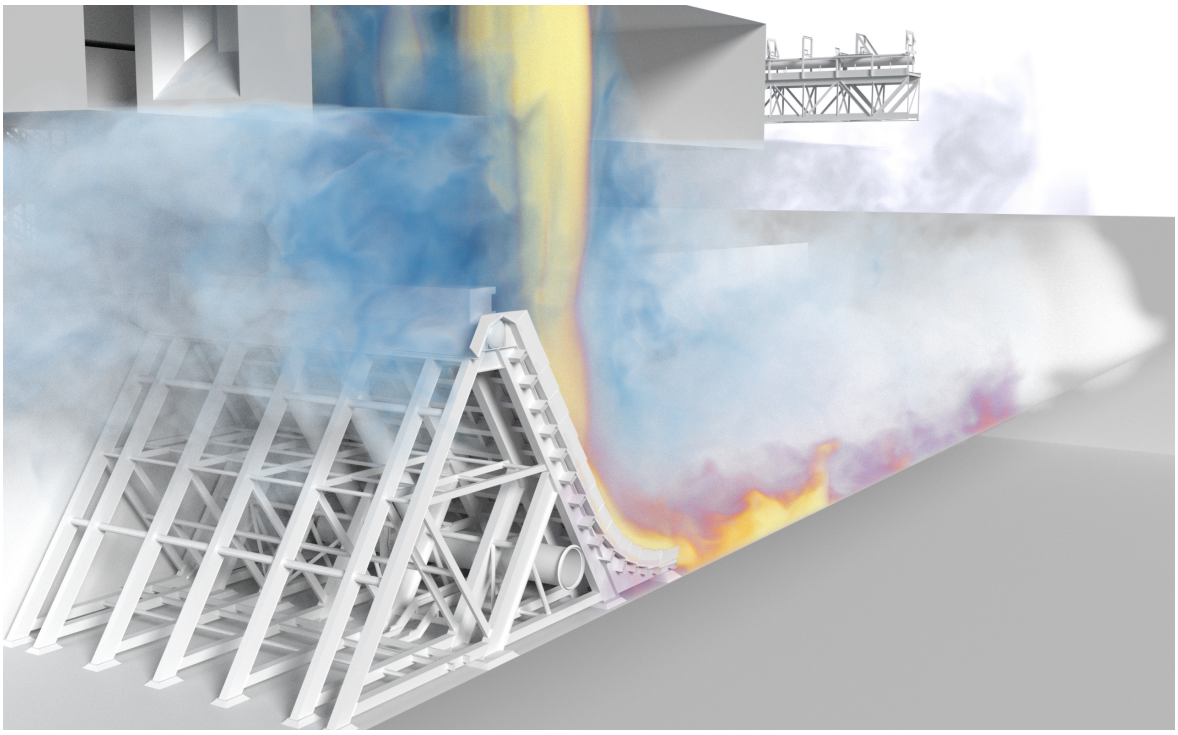

Fig. 15 View of plume (yellow/purple), liquid water (blue), and water vapor (white) mass fractions from behind the flame deflector. Some geometry has been hidden for clarity.

strength. Figure 17 shows the sound pressure level versus frequency for the same three probes. The bottom plot for the probe near the exhaust duct shows a clear reduction in sound pressure level across all frequencies when the water system is active. Sensors at the top of the booster and in the payload area also show a reduction in sound pressure level across a large frequency range.

To address the issue raised in the SLS program regarding pressure loads on the mobile launch pad we now look at surface data extracted from our simulations. Figure 18 shows a side-by-side comparison of the maximum pressure over time for the entire simulation durations. The plot on the left shows the was without sound suppression water and the plot on the right shows the results when the water system is active. Right of the exhaust duct we observe a large maximum pressure in the dry case. In the case with water we no longer observe this “hot-spot” and furthermore, comparing the distribution of the maximum pressure on the surface we see a significantly reduced max nearly everywhere. These results indicate the water system is reducing the acoustic loads underneath the launch pad.

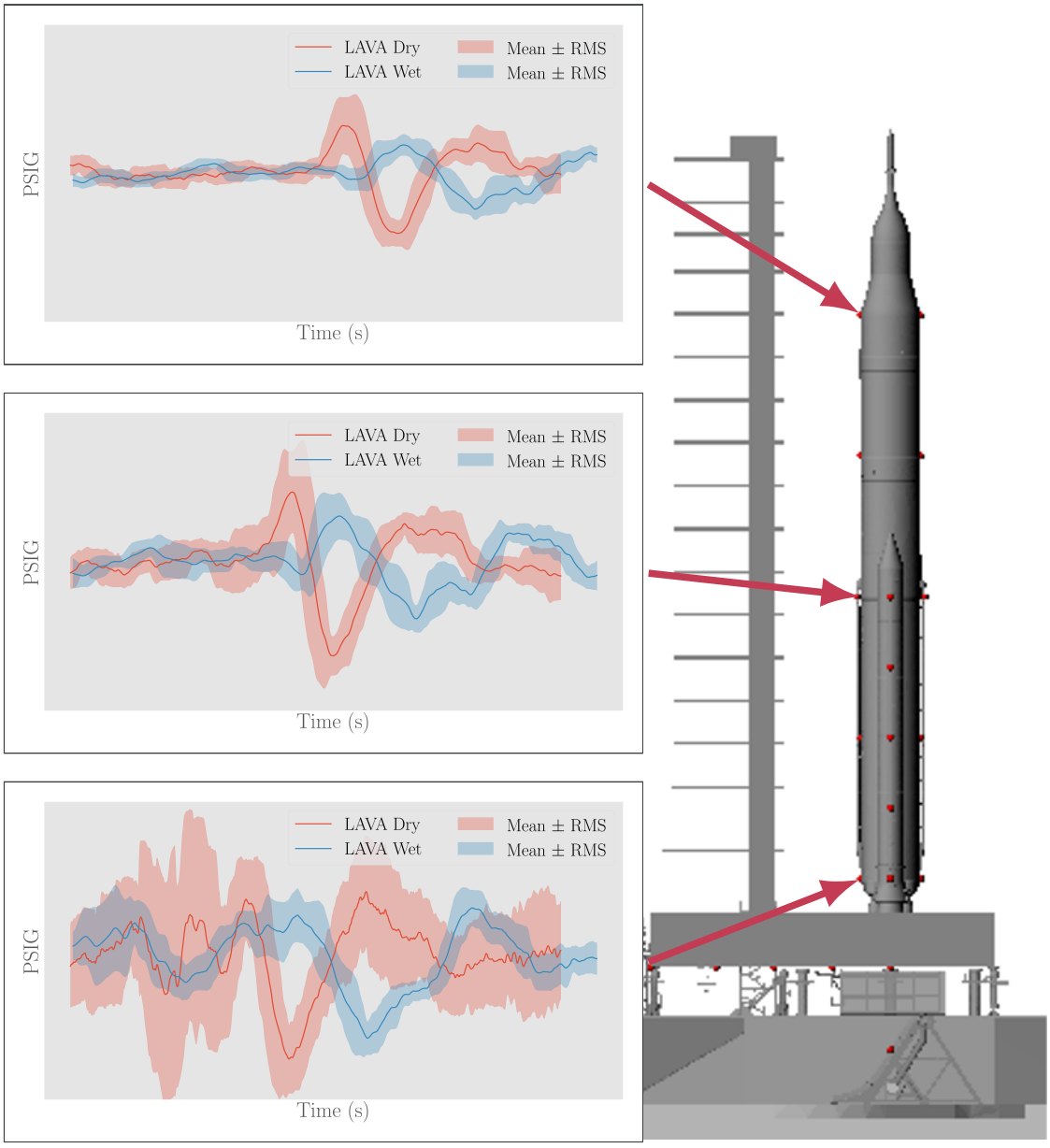

Fig. 16 Pressure signals on vehicle for cases with and without sound suppression water. Plots are drawn using the same scale.

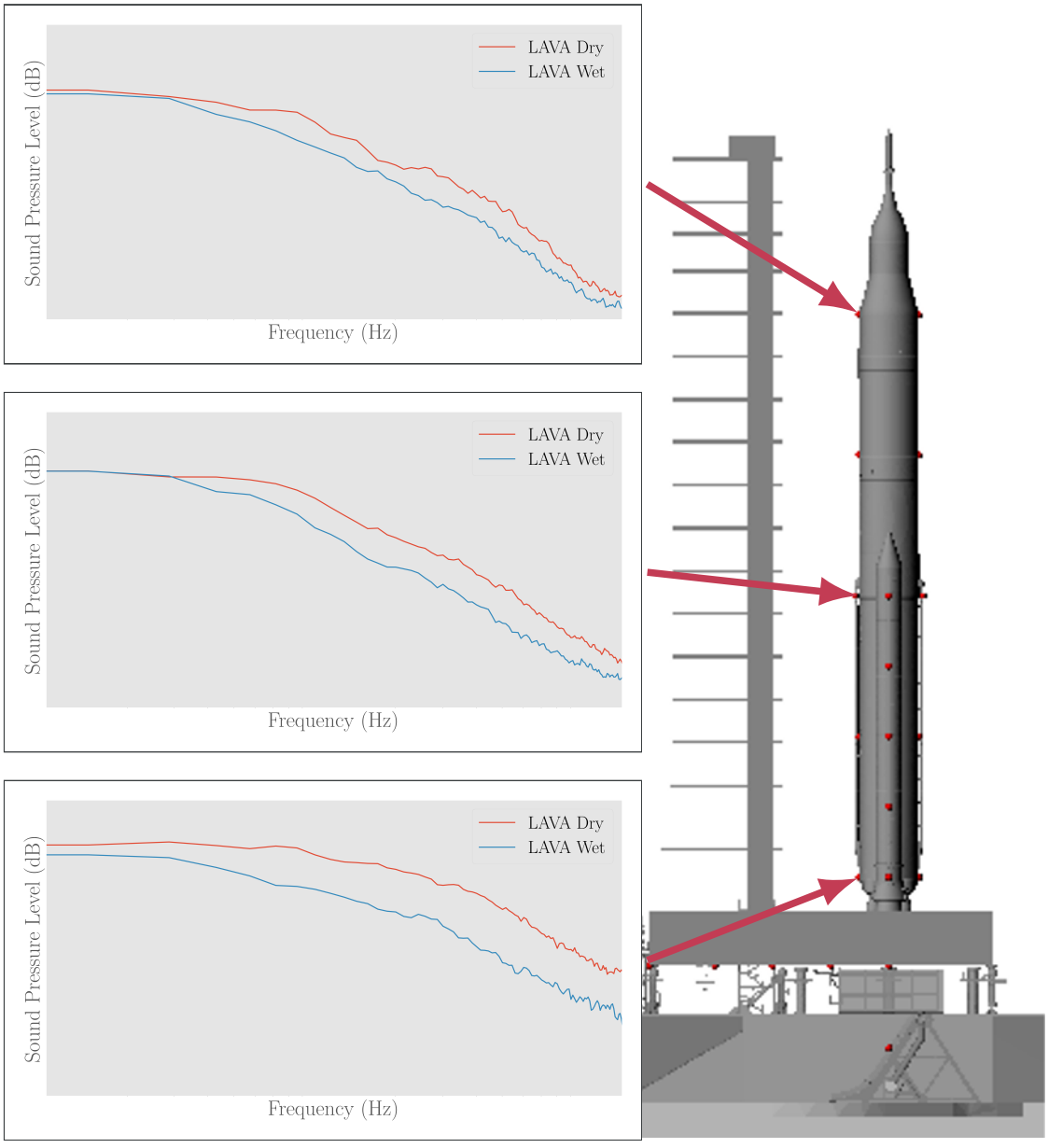

Fig. 17 Sound pressure levels on the vehicle for cases with and without sound suppression water. Plots are drawn using the same scale.

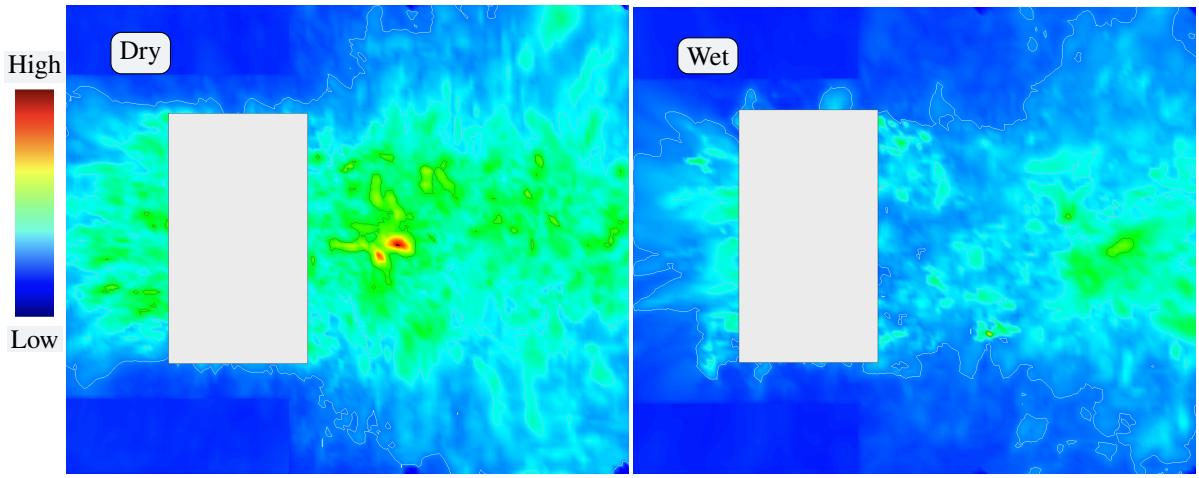

Fig. 18 Maximum instantaneous pressures on the bottom of the mobile launcher over the full simulation without water (left) and with water (right). The surfaces are colored using the same scale.

V. Summary

We have presented applications of a novel methodology for predicting IOP propagation in launch environments which include water-based sound suppression systems using NASA's LAVA Cartesian immersed boundary framework. Unique characteristics for this multiphase method are the use of high order method with provable robustness that can remain stable in the extreme launch environment conditions. Using an immersed boundary framework makes including the complex geometry of launch vehicles and support structures relatively simple which is especially useful to accommodate changes that may occur during design. We have also presented a validation case of LAVA's multiphase capability using the SLS Scale Model Acoustic Test considering two cases, a dry case and a case with water systems active. The dry simulation results showed excellent agreement with measured pressure signals and demonstrated that the boundary conditions and computational mesh were adequate for reproducing the experiment. Considering the simulation with water systems active, the results are convincing that the solver can predict IOP phenomena although we noted some discrepancies in our computed results compared to sensor measurements. In light of the very accurate dry results, the discrepancies observed in the simulation with water systems active can likely be attributed to the modeling of the water injection system. As noted in the previous sections, including the water systems introduces a number of new challenges. Chief among these challenges is getting an accurate spatial distribution of water prior to booster ignition. The water system is active well before the engines are started which thoroughly floods the exhaust hole and flame trench. Reproducing this environment prior to engine ignition would be too computationally expensive for our present solver so we chose to start the water system simultaneously with the liquid engines. Future work may include some implicit time stepping procedure or low-Mach preconditioning that would increase the maximum stable time step and make simulating the low-speed water more practical.

After completing the SLS SMAT validation case, we turned towards the problem of simulating the full-scale SLS vehicle including the IOP/SS on the redesigned mobile launcher (ML). The results for SLS at LC-39B showed a large reduction in the IOP signal at pressure sensors located on the vehicle body. Additionally, we compared the overall sound pressure level at these sensors and observed the noise reduction effect from the IOP/SS. The effect of the IOP/SS was also observed on the ML which showed greatly reduced maximum overpressure for the case which the IOP/SS is active versus a hypothetical "dry fire" case. These results were briefed to KSC engineers and used to evaluate the flight readiness of the mobile launcher prior to the Artemis I mission. Once Artemis I flight data is available we plan to make direct comparisons and assess the accuracy of these results.

Acknowledgements

This work was partially supported by NASA KSC Exploration Ground Systems (EGS). We would like to acknowledge NASA Launch Service Program (LSP) for their collaboration with our launch environment simulations. Computer time has been provided by the NASA Advanced Supercomputing (NAS) facility at NASA Ames Research Center. We also want to acknowledge the SLS program for their support.

Appendix

A. Validation of the Fractional Algorithm Coupled with the Phase Transition Solver

The approximate thermo-chemical relaxation approach proposed by Chiapolino et al. [23] is implemented and used in this work as the phase transition solver. The fractional algorithm composed of the hyperbolic time stepping and thermal relaxation is followed by the approximate phase transition solver in this work. The approximate model has the robustness advantage over the exact solver for the thermo-chemical relaxation, while is still shown to be accurate. We have also improved the robustness of the approximate thermo-chemical relaxation approach with further limiting of the final solutions from the original approximate solver using the initial state passed to the solver such that the mass fractions and volume fractions are bounded, and numerical failures due to negative squared mixture sound speed can be prevented. The fractional algorithm with the approximate phase transition solver is validated using three different 1D shock tube test problems proposed in [23]. While the more general equation of state, Noble-Abel-Stiffened-Gas [24] was used in the original tests, we only use the stiffened gas equation of state to ensure the robustness of the algorithm. The properties of liquid water and water vapor used in this section are given in Table 1.

The first shock tube test problem consists of a two-phase mixture with initial liquid water, water vapor, and air mass fractions uniformly set to $Y_1 = 0.1$, $Y_2 = 0.2$, and $Y_3 = 0.7$ respectively in a domain $[-1, 1]$ m. There is a discontinuity with a pressure ratio of two initially located in the middle of the domain, where the left and right portions have pressure $p_L = 0.2$e6Pa and $p_L = 0.1$e6 Pa respectively. The initial temperature is obtained with the assumption of thermo-chemical equilibrium, where an iterative solve to satisfy

$$T = T_{sat}(x_v p),\ x_v = \frac{Y_2/W_2}{Y_2/W_2 + \sum_{k=3}^{N} Y_k/W_k}. \tag{11}$$

The saturation temperature T_{sat} is obtained by equating the Gibbs free energies of the liquid water and water vapor using the vapor mole fraction x_v and the initial pressure. The results of the fractional algorithm using WCNS-IS combined with the approximate phase transition solver at $t = 1.0$e-3 s are shown in figure 19 with two different grid resolutions. The reference solution is obtained with the four-equation HRM coupled with the approximate phase transition solver using first order HLLC scheme on a much finer mesh composed of 200000 grid points. It can be seen that the solutions of fractional algorithm compare well with the reference solutions and the solutions converge towards the reference solutions with grid refinement.

The next two shock tube test problems have mixtures mainly composed of air and water respectively in the same domain. In these two problems, the initial conditions have the pressure jump as same as the first problem but with uniform temperature at 293 K. $Y_3 = 0.98$ and $Y_3 = 1$e-5 are set respectively in these two problems such that the second test has air as the major constituent of the mixture while the third test has water (combined liquid water and water vapor) as the major component. The saturation pressure, $p_{sat} = x_v p$, as well as the liquid water and water mass fractions can be deduced using the liquid and vapor Gibbs free energy equality under the thermo-chemical assumption. Figures 20 and 21 respectively shows the results of the second and third test problems using the fractional algorithm coupled with the approximate phase transition solver. Good grid convergence towards the reference solutions can be observed at the end of the simulations using our proposed approach. Overall, these shock tube test problems with phase transition show the accuracy and robustness of the approach using the fractional algorithm with WCNS-IS in [17] and the approximate phase transition solver extended from [23].

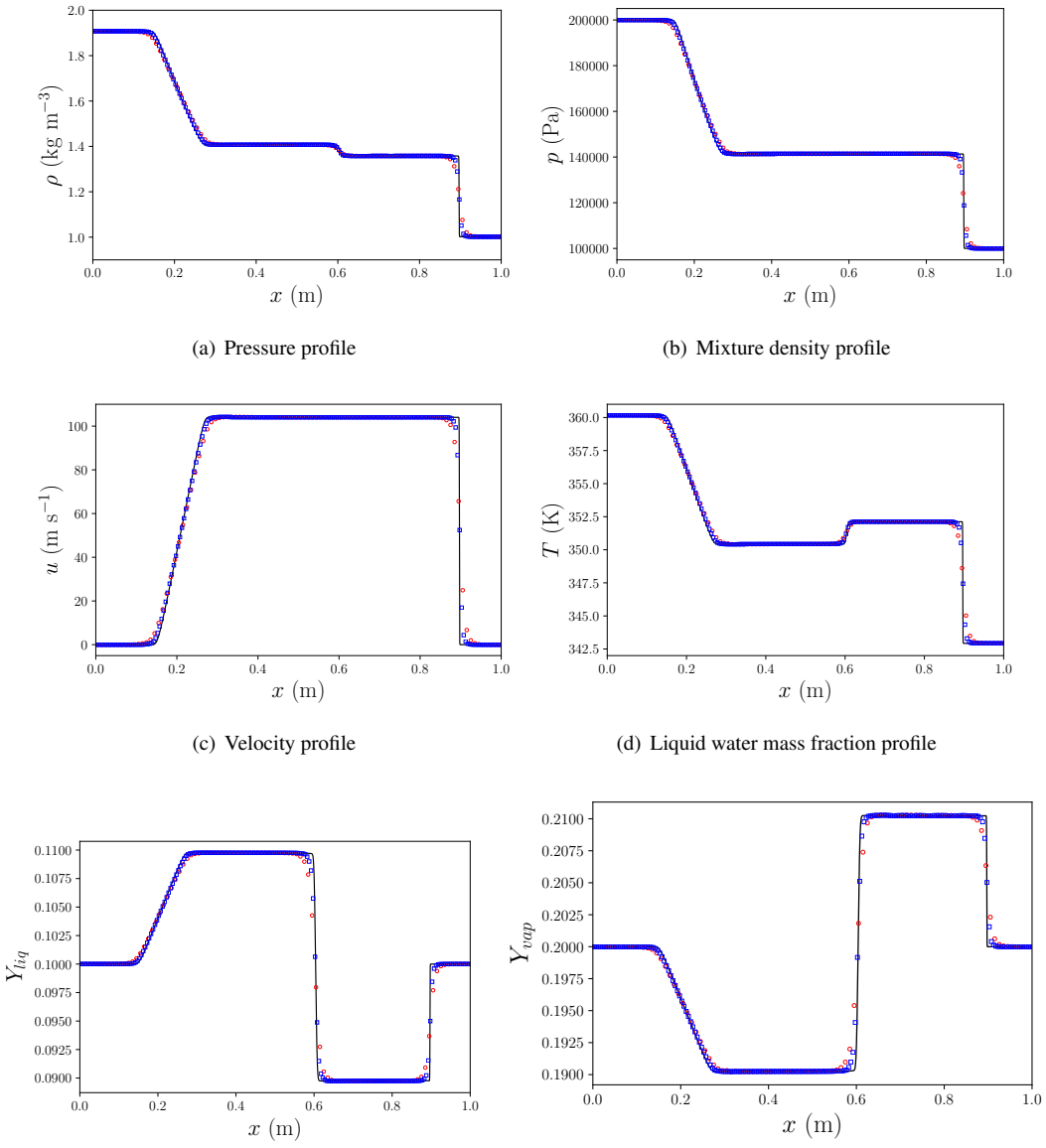

(a) Pressure profile

(b) Mixture density profile

(c) Velocity profile

(d) Liquid water mass fraction profile

(e) Water vapor mass fraction profile

(f) Air mass fraction profile

Fig. 19 First 1D phase transition problem at t = 1e−3 s using different flow models and schemes. Black solid line: reference solutions (four-equation HRM with approximate phase transition solver using first order HLLC scheme with 200000 points); red circles: fractional algorithm with approximate phase transition solver using WCNS-IS with 100 points; blue squares: fractional algorithm with approximate phase transition solver using WCNS-IS with 200 points.

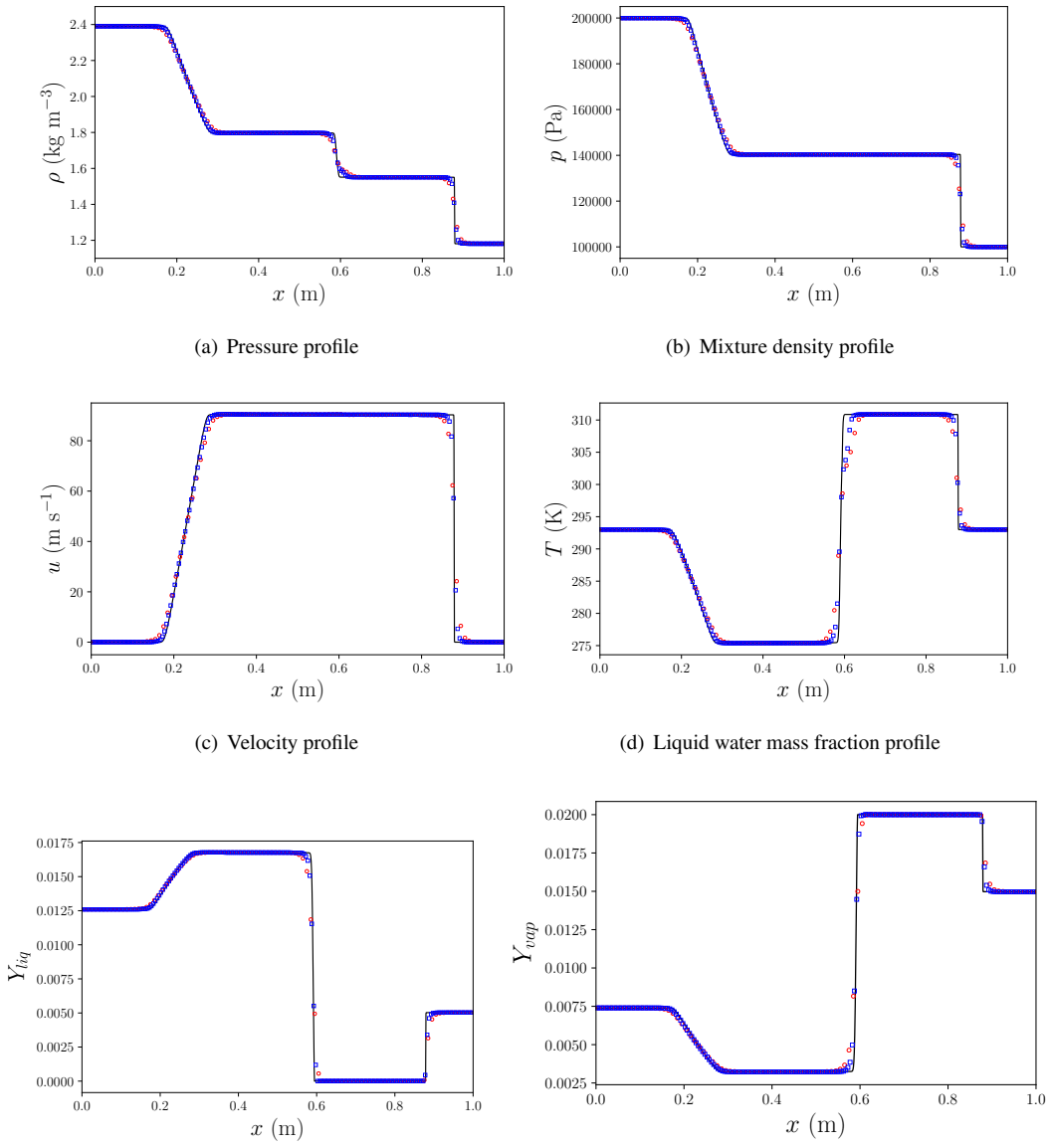

(a) Pressure profile

(b) Mixture density profile

(c) Velocity profile

(d) Liquid water mass fraction profile

(e) Water vapor mass fraction profile

(f) Air mass fraction profile

Fig. 20 Second 1D phase transition problem at t = 1e−3 s using different flow models and schemes. Black solid line: reference solutions (four-equation HRM with approximate phase transition solver using first order HLLC scheme with 200000 points); red circles: fractional algorithm with approximate phase transition solver using WCNS-IS with 100 points; blue squares: fractional algorithm with approximate phase transition solver using WCNS-IS with 200 points.

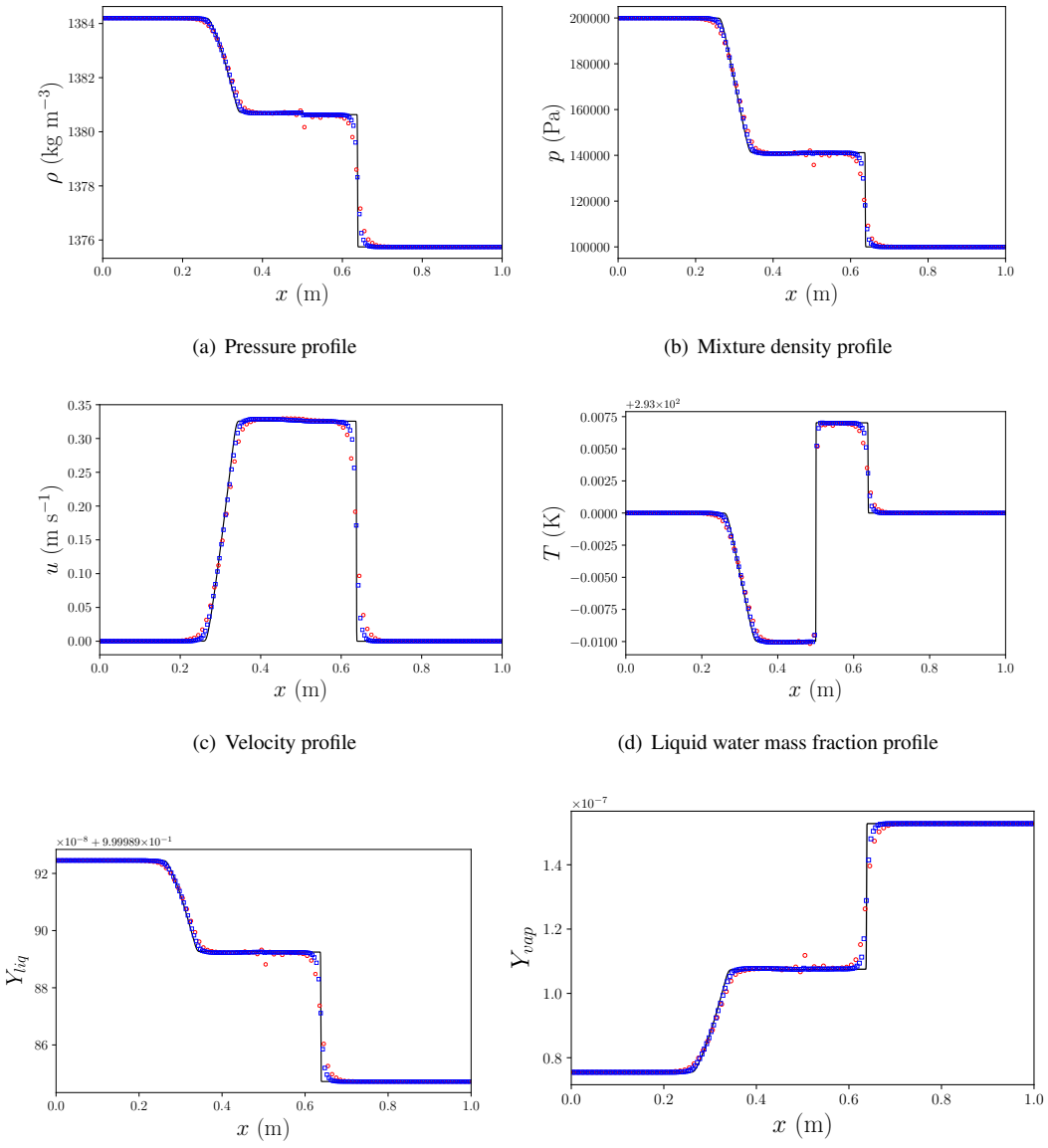

(a) Pressure profile

(b) Mixture density profile

(c) Velocity profile

(d) Liquid water mass fraction profile

(e) Water vapor mass fraction profile

(f) Air mass fraction profile

Fig. 21 Third 1D phase transition problem at t = 1.5e−3 s using different flow models and schemes. Black solid line: reference solutions (four-equation HRM with approximate phase transition solver using first order HLLC scheme with 200000 points); red circles: fractional algorithm with approximate phase transition solver using WCNS-IS with 100 points; blue squares: fractional algorithm with approximate phase transition solver using WCNS-IS with 200 points.

References

[1] Eldred, K. M., "Acoustic loads generated by the propulsion system," Monograph NASA SP-8072, National Aeronautics and Space Administration, 1971.

[2] Plotkin, K., Sutherland, L., and Vu, B., *Lift-Off Acoustics Predictions for the Ares I Launch Pad*, 2009. https://doi.org/10.2514/6.2009-3163, URL https://arc.aiaa.org/doi/abs/10.2514/6.2009-3163.

[3] West, J., Strutzenberg, L., Putnam, G., Liever, P., and Williams, B., "Development of modeling capabilities for launch pad acoustics and ignition transient environment prediction," *18th AIAA/CEAS Aeroacoustics Conference (33rd AIAA Aeroacoustics Conference)*, 2012, p. 2094.

[4] Harris, R. E., Collins, E. M., Luke, E. A., and Sescu, A., "Coupled Overset Unstructured Discontinuous Galerkin Method for Launch Environment Acoustics Prediction," *AIAA Journal*, Vol. 54, No. 6, 2016, pp. 1932–1952. https://doi.org/10.2514/1.J054563, URL https://doi.org/10.2514/1.J054563.

[5] Troyes, J., Vuillot, F., Langenais, A., and Lambaré, H., "Coupled CFD-CAA Simulation of the Noise Generated by a Hot Supersonic Jet Impinging on a Flat Plate with Exhaust Hole," 2019.

[6] Xing, C., Le, G., Shen, L., Zhao, C., and Zheng, H., "Numerical investigations on acoustic environment of multi-nozzle launch vehicle at lift-off," *Aerospace Science and Technology*, Vol. 106, 2020, p. 106140. https://doi.org/https://doi.org/10.1016/j.ast.2020.106140, URL https://www.sciencedirect.com/science/article/pii/S1270963820308221.

[7] Fujii, K., Nonomura, T., and Tsutsumi, S., "Toward accurate simulation and analysis of strong acoustic wave phenomena-A review from the experience of our study on rocket problems," *International Journal for Numerical Methods in Fluids*, Vol. 64, 2010, pp. 1412–1432.

[8] Kiris, C. C., Housman, J. A., Barad, M. F., Brehm, C., Sozer, E., and Moini-Yekta, S., "Computational framework for Launch, Ascent, and Vehicle Aerodynamics (LAVA)," *Aerospace Science and Technology*, Vol. 55, 2016, pp. 189–219. https://doi.org/https://doi.org/10.1016/j.ast.2016.05.008, URL https://www.sciencedirect.com/science/article/pii/S127096381630178X.

[9] Tsutsumi, S., Shimizu, T., Takaki, R., Shima, E., Fujii, K., and Arita, M., "Numerical study of pressure waves generated by H-IIA launch vehicle at lift-off," *Proceedings of the Korean Society of Propulsion Engineers Conference*, The Korean Society of Propulsion Engineers, 2008, pp. 266–271.

[10] Tsutsumi, S., Takaki, R., Nakanishi, Y., Okamoto, K., and Teramoto, S., "Acoustic generation mechanism of a supersonic jet impinging on deflectors," *52nd Aerospace Sciences Meeting*, 2014, p. 0882.

[11] Tatsukawa, T., Nonomura, T., Oyama, A., and Fujii, K., "Nozzle-to-ground distance effect on nondominated solutions of multiobjective aeroacoustic flame deflector design problem," *21st AIAA/CEAS Aeroacoustics Conference*, 2015, p. 2683.

[12] Housman, J., Barad, M., and Kiris, C., *Space-Time Accuracy Assessment of CFD Simulations for the Launch Environment*, 2011. https://doi.org/10.2514/6.2011-3650, URL https://arc.aiaa.org/doi/abs/10.2514/6.2011-3650.

[13] Wong, M. L., Angel, J. B., Barad, M. F., and Kiris, C. C., "A positivity-preserving high-order weighted compact nonlinear scheme for compressible gas-liquid flows," *Journal of Computational Physics*, Vol. 444, 2021, p. 110569. https://doi.org/https://doi.org/10.1016/j.jcp.2021.110569, URL https://www.sciencedirect.com/science/article/pii/S0021999121004642.

[14] Ryan, R. S., Jones, J. H., Guest, S. H., Struck, H. G., Rheinfurth, M. H., and Verferaime, V. S., "Propulsion System Ignition Overpressure for the Space Shuttle," Tech. rep., NASA, 1981.

[15] Stuckey, J., and Heiney, A., "Sound Suppression Test Unleashes a Flood," , Sept 2008. URL https://www.nasa.gov/missions/shuttle/f_watertest.html.

[16] Allaire, G., Clerc, S., and Kokh, S., "A five-equation model for the simulation of interfaces between compressible fluids," *Journal of Computational Physics*, Vol. 181, No. 2, 2002, pp. 577–616.

[17] Wong, M. L., Angel, J. B., and Kiris, C. C., "A positivity-preserving Eulerian two-phase approach with thermal relaxation for compressible flows with a liquid and gases," *Submitted*, 2022.

[18] Deng, X., and Zhang, H., "Developing high-order weighted compact nonlinear schemes," *Journal of Computational Physics*, Vol. 165, No. 1, 2000, pp. 22–44.

[19] Nonomura, T., Iizuka, N., and Fujii, K., "Increasing order of accuracy of weighted compact nonlinear scheme," *AIAA Paper*, Vol. 893, 2007.

[20] Zhang, S., Jiang, S., and Shu, C.-W., "Development of nonlinear weighted compact schemes with increasingly higher order accuracy," *Journal of Computational Physics*, Vol. 227, No. 15, 2008, pp. 7294–7321.

[21] Wong, M. L., and Lele, S. K., "High-order localized dissipation weighted compact nonlinear scheme for shock-and interface-capturing in compressible flows," *Journal of Computational Physics*, Vol. 339, 2017, pp. 179–209.

[22] Shu, C.-W., and Osher, S., "Efficient implementation of essentially non-oscillatory shock-capturing schemes, II," *Journal of Computational Physics*, Vol. 83, No. 1, 1989, pp. 32–78.

[23] Chiapolino, A., Boivin, P., and Saurel, R., "A simple and fast phase transition relaxation solver for compressible multicomponent two-phase flows," *Computers & Fluids*, Vol. 150, 2017, pp. 31–45.

[24] Le Métayer, O., and Saurel, R., "The Noble-Abel stiffened-gas equation of state," *Physics of Fluids*, Vol. 28, No. 4, 2016, p. 046102.

[25] Davidson, M., "Quiet, Please: NASA Engineers Wrapping Up Acoustic Testing for Space Launch System," , Aug 2014. URL https://www.nasa.gov/sls/sls-smat-test-aug2014.html.

[26] Le Métayer, O., Massoni, J., Saurel, R., SMASH, P., et al., "Elaborating equations of state of a liquid and its vapor for two-phase flow models; Elaboration des lois d'etat d'un liquide et de sa vapeur pour les modeles d'ecoulements diphasiques," *International journal of thermal sciences*, Vol. 43, 2004.